Reddy, S.M., Timms, N.E., Pantleon, W. & Trimby, P. (2007). Quantitative characterization of plastic deformation of zircon and geological implications. Contributions to Mineralogy and Petrology, 153, 625-645.

Quantitative Characterization of Plastic Deformation of Zircon and Geological Implications

Steven M. Reddy[1]*, Nicholas E. Timms[1], Wolfgang Pantleon[2] & Patrick Trimby[3]

[1] The Institute for Geoscience Research, Dept of Applied Geology, Curtin University of Technology, GPO Box U1987, Perth, WA 6845, Australia

[2] Materials Research Department, Risø National Laboratory, Frederiksborgvej 399, 4000 Roskilde, Denmark

[3] HKL Technology A/S, Majsmarken 1, 9500 Hobro, Denmark. Now at: LINK Nordiska AB, LINK Analytical AB, Lejonvägen 28, 181 22 Lidingö, Sweden

Key Words: Zircon, EBSD, microstructure, low-angle boundaries, slip system, dislocation, accessory phase, diffusion, dissolution.

* Corresponding author.

E-mail address: S.Reddy@curtin.edu.au
fax: +61-8-9266-3153
Tel.:+61-8-9266-4371

Acknowledgements: The Australian Research Council (via Grants R00107937**,** LX0453429 & DP0664078), Curtin University (via a Targeted Research Fellowship to SMR) and the Tectonics SRC are thanked for funding this research. John Terlet and Peter Self are thanked for providing access to the Adelaide EBSD system. Bob Pidgeon, Paul Evins and an anonymous reviewer are thanked for constructive reviews of the manuscript. This paper is The Institute for Geoscience Research (TIGeR) publication No. 3.

Abstract

The deformation-related microstructure of an Indian Ocean zircon hosted in a gabbro deformed at amphibolite-grade has been quantified by electron backscatter diffraction. Orientation mapping reveals progressive variations in intragrain crystallographic orientations that accommodate 20° of misorientation in the zircon crystal. These variations are manifest by discrete low-angle (<4º) boundaries that separate domains recording no resolvable orientation variation. The progressive nature of orientation change is documented by crystallographic pole figures which show systematic small circle distributions, and disorientation axes associated with 0.5-4° disorientation angles, which lie parallel to rational low index crystallographic axes. In the most distorted part of the grain (area A), this is the [100] crystal direction. A quaternion analysis of orientation correlations confirms the [100] rotation axis inferred by stereographic inspection, and reveals subtle orientation variations related to the local boundary structure. Microstructural characteristics and orientation data are consistent with the low-angle boundaries having a tilt boundary geometry with dislocation line [100]. This tilt boundary is most likely to have formed by accumulation of edge dislocations associated with a <001> {100} slip system. Analysis of the energy associated with these dislocations suggest they are energetically more favourable than TEM verified <010>{100} slip. Analysis of minor boundaries in area A indicates deformation by either $\left[0\bar{1}0\right]$ (001) edge, or [100](100) and [001](100) screw dislocations. In other parts of the grain, $\left[1\bar{1}0\right]$ cross slip on (111), $\left(11\bar{1}\right)$ and (112) planes seems likely. These data provide the first detailed microstructural analysis of naturally deformed zircon and indicate ductile crystal-plastic deformation of zircon by the formation and migration of dislocations into low-angle boundaries. Minimum estimates of dislocation density in the low-angle boundaries are of the order of $\sim3.10^{10}$ cm^{-2}. This value is sufficiently high to have a marked effect on the geochemical behaviour of zircon, via enhanced bulk diffusion and increased dissolution rates. Therefore, crystal plasticity in zircon may have significant implications for the interpretation of radiometric ages, isotopic discordance and trace element mobility during high-grade metamorphism and melting of the crust.

Zircon ($ZrSiO_4$) is an extremely significant accessory phase due to its ability to incorporate and retain geologically important trace and rare earth elements (REE), including elements produced by radioactive decay. These characteristics enable the geochemistry of zircon to be applied to a wide range of geoscience disciplines, for example rock petrogenesis (Belousova et al. 2002; Hoskin and Schaltegger 2003; Hawkesworth and Kemp 2006); metamorphic processes (Fitzsimons et al. 1997; Schaltegger et al. 1999; Rubatto and Hermann 2003), sedimentary provenance (Hoskin and Ireland 2000; Cawood et al. 2003), geothermometry (Watson and Harrison 2005), and crustal recycling studies, including the evolution of early Earth using stable isotopes of oxygen (Mojzsis et al. 2001; Wilde et al. 2001). The broad application of zircon geochemistry and geochronology to a range of igneous, sedimentary and metamorphic rocks has also provided valuable constraints on the tectonic events that are responsible for their formation (e.g., DeCelles et al. 2000; Whitehouse and Platt 2003; Collins et al. 2004; Dempster et al. 2004).

Key to the extensive use of zircon is its assumed physical and chemical durability. The refractory behavior of zircon is supported by empirical evidence that zircon can preserve geochemical information and primary growth zoning through cycles of weathering and sedimentation, high-grade metamorphism and even entrainment in igneous rocks (Gulson and Krogh 1973; Pankhurst and Pidgeon 1976; Ross et al. 1992; Lanyon et al. 1993; Rubatto et al. 2001; Cawood et al. 2003). Experimental data show that diffusion of trace and REE in zircon in pristine zircon requires extremely high temperatures (>900°C) (Cherniak et al. 1997b; Lee et al. 1997; Connelly 2000), as does the diffusion of oxygen under dry conditions (Valley 2003). However, many studies indicate element mobility (particularly Pb loss) in zircon at lower temperatures than predicted by diffusion experiments (Gebauer and Grünenfelder 1976; Pidgeon and Compston 1992; Geisler et al. 2002). This is commonly interpreted to reflect recrystallization and annealing of the zircon lattice following radiation damage (metamictization) (Silver 1964; Pidgeon and Compston 1992; Mezger and Krogstad 1997; Geisler 2002). However one recently demonstrated and potentially important process is enhanced bulk diffusion caused by the development of fast-diffusion pathways associated with plastic deformation microstructures in zircon (Reddy et al. 2006).

Despite empirical data that illustrate a relationship between crystal-plastic microstructures and geochemistry (Reddy et al. 2006), there are few detailed studies on the microstructural characterization of plastically deformed zircon. Indeed, the only detailed account of crystal-plastic deformation in zircon has concentrated on transmission electron microscopy (TEM) to recognize glide systems that developed as a result of experimental shock deformation (Leroux et al. 1999)(Table 1). This study attempts to rectify this by quantifying deformation-related microstructures in zircon using electron backscatter diffraction (EBSD) in the scanning electron microscope (SEM) (Prior et al. 1999; Schwartz et al. 2000). Such an approach has lead to significant advances in the understanding of grain-scale deformation processes and mechanisms in major rock-forming minerals, for example, enabling intragrain crystallographic variations to be used to determine active glide systems (e.g., Lloyd and Freeman 1994; Lloyd et al. 1997; Boyle et al. 1998; Bestmann and Prior 2003; Reddy and Buchan 2005). The detailed microstructural examination presented here develops this approach for accessory phases, provides new data regarding the natural plastic deformation of zircon, and addresses the significance of zircon deformation for geological research.

Geological Background

The analyzed zircon comes from olivine gabbro (Sample 176-735B-162R-6-22-24) collected from core recovered during Ocean Drilling Program (ODP) Leg 176 from Hole 735B. The core represents a sample of the ultra-slow spreading Southwest Indian Ridge (32º43.392'S, 57º15.960'E) (Fig. 1a) and was drilled in a mean water depth of 735m. The core comprises predominantly of gabbro or olivine gabbro that can be characterized by a number of different litho-stratigraphic units (Units I-XII) (Dick et al. 2000)). The sample was collected from unit XI, 1089m below the sea floor. Results from leg 176 show the cored oceanic crust to record a complex deformation history, with different units displaying heterogeneous deformation characterized by syn-magmatic and sub-solidus high-temperature crystal-plastic deformation through to brittle fracture and cataclasis (Dick et al. 2000; Bach et al. 2001). Discontinuous granulite- to amphibolite-grade (1000-600˚C) deformation fabrics are cut by semi-brittle and brittle low temperature shear zones as strain was localized into a system of discrete low-angle detachment faults during greenschist- and subgreenschist-grade (<500˚C) conditions (John et al. 2004). The deformation represents dynamic uplift and denudation of oceanic crust (John et al. 2004). Detailed petrologic and thermochronologic analysis of this area of oceanic crust indicates initial crystallization at 11.93 ± 0.14 Ma, followed by relatively rapid cooling such that the crust had cooled below 500°C by 11.3 Ma (John et al. 2004; Schwartz et al. 2005).

Analytical Procedure

A petrographic thin section of the rock sample was polished with progressively finer grades of diamond paste (0.25μm) followed by a further 4 hours of polishing with 0.06μm colloidal silica in a NaOH solution (pH10). EBSD data were collected from a single zircon grain found within the thin section using different SEMs housed at Curtin University of Technology and University of Adelaide in Australia and HKL Technology labs in Denmark. SEM settings used for data collection are documented in Table 2. Automatic EBSD mapping was undertaken by collecting and indexing an EBSP from each node of a user-defined grid. Several different areas of the zircon grain were analyzed at different spatial resolutions (for details see Table 2). Acquisition of EBSD data was undertaken using HKL Technology's Channel 5 Flamenco software using the parameters documented in Table 2.

Empirically obtained EBSPs from the zircon were automatically indexed to theoretical (hkl) reflector intensities of the different Kikuchi bands of zircon. The theoretical reflector intensity file was derived from Channel 5 Twist software via structure factor calculations that utilize a kinematical electron diffraction model. Information required for this calculation (crystallography, space group, atom coordinate and occupancy data) were obtained from the Mincryst crystallographic and crystallochemical database (Card No 5260) (Chichagov et al. 2001), which summarizes data originally collected by Hazen & Finger (1979) (Table 3). Although there are numerous possible crystallographic datasets that can be used to generate theoretical reflector files for zircon, a detailed examination of 23 of these using zircons collected from a range of geological environments (Reddy, unpublished data) indicates that the parameters in Table 3 yield consistently high indexing of good quality.

For all data, the angular "closeness of fit" between the empirically obtained pattern and the theoretical solution, quoted as the mean angular deviation (MAD), was generally good, i.e. low (Table 2). MADs greater than 1.3 were rejected as poor quality fits. For some maps an "orientation lock" (setting 4) was used to refine solutions and provide more accurate orientation data (Table 2).

The EBSD data from each area was processed in different ways to produce a series of maps that show different aspects of the microstructure. Maps (with the exception of Fig. 6c & 7c) were produced using the Channel 5 "Tango" module. All EBSD data were noise reduced using a "wildspike" correction and a five-neighbor zero solution extrapolation. Data were also passed once through a modified Kuwahara filter (Humphreys et al. 2001) made available in Channel 5 Service Pack 8. In all cases a 3x3 filter size with 5° smoothing angle and a 1° artifact angle was used. Such a filter can produce artifacts in the data particularly around grain boundaries. Comparison of misorientation axis maps and stereographic projections with and without the modified Kuwahara filter (not shown) indicate a significant noise reduction for 0.5-1° boundaries when the filter is used and no significant artifact generation.

Band contrast is obtained from an assessment of the contrast identified in the Hough transform, and is a measurement of pattern quality that is a fundamental property of the EBSP. Band contrast is susceptible to variations in crystallographic orientation, structural integrity, crystal damage and surface topography and is therefore particularly useful for qualitatively delimiting the sample microstructure. During data processing, band contrast maps were therefore used as a background over which phase or orientation data were draped. Phase maps were produced by assigning a different color to each identified phase. A map of plagioclase grain area was produced using a 10˚ minimum boundary cut off. Orientation maps were produced using the Channel 5 'texture' component in which each pixel is colored for minimum misorientation relative to a user-defined reference orientation. Local misorientation maps illustrate the mean of the minimum misorientations between a central pixel and each surrounding pixel in a 3x3 grid; the mean being assigned to the central pixel.

Crystallographic orientation and misorientation data were plotted using Channel 5 "Mambo" software using lower hemisphere, equal area projections. All data are reported with respect to an arbitrarily assigned X-Y coordinate framework for the sample surface that is also shown in each of the orientation maps. Crystallographic axes of the zircon grain were arbitrarily assigned specific miller indices in the sample reference frame to facilitate description and interpretation of the data.

The tetragonal crystal symmetry of zircon means that eight possible misorientation angle/axes may be calculated between two different crystallographic orientations (Grimmer 1980). In this study, the angle/axis pair corresponding to the minimum misorientation angle (referred to as "disorientation" in the materials literature and henceforth in this paper) was used for analysis. This can be justified because the changes in misorientation are progressive and can be mapped continuously from the undeformed core of the zircon. It should be noted that angular errors associated with disorientation axis calculations can be up to ± 30° for 2° disorientations, and will vary with angular resolution (MAD) of the data (Prior 1999).

The orientation information stored in the EBSD data from Area A were also analyzed using the principles detailed by Pantleon (2005). This approach uses the unit quaternion description of m discrete orientations, q_i (i=1…m) to define the mean orientation. A summary of the relationships between unit quaternions, and the commonly used angle/axis pair and Euler notations are outlined in Appendix 1. The disorientations ($\delta q_i = q_i \overline{q}^{-1}$) of all individual orientations (q_i) from the mean ($\overline{q}$) can be calculated. The spread of all orientations can then be characterized by a symmetric tensor (Q) that allows subsequent calculation of three non-negative eigenvalues. The eigenvector corresponding to the maximum eigenvalue characterizes the dominant rotation axis (Pantleon 2005). This methodology has the advantage that the definition of the dominant rotation axis is unambiguous and allows a sign to be assigned to all disorientation angles. Orientation gradients associated with grain scale bending of the crystal lattice can also be removed to allow details of the orientation variations within the microstructure to be resolved. This is important in situations where the underlying microstructure comprises alternating disorientations of different sign. As an additional benefit, the unpredictable problem of microstructure concealment due to arbitrary selection and application of color schemes to orientation maps can be eliminated. This approach therefore compliments the more widely used approach of inspection of dispersion or disorientation axes on stereographic projections and provides a more qualitative assessment of dominant rotation axes associated with intragrain disorientations.

Microstructural Analysis of Zircon

The studied zircon is a single grain that has a long axis of *c.*700μm (Fig. 1b) and resides within a fine-grained, polymineralic matrix dominated by plagioclase and magnetite (Fig. 1c). The matrix is strongly deformed and represents a high-strain zone between two large phenocrysts of orthopyroxene and plagioclase (Fig. 1b). Dynamic recrystallization of the matrix is evident by a shape-preferred orientation of plagioclase and a noticeable reduction in the grain size of recrystallized plagioclase around the tips of the zircon grain (Fig. 1d).

Orientation contrast imaging (Prior et al. 1996) reveals greyscale changes that indicate crystallographic orientation variations across the zircon grain (Fig. 2a). Gradual orientation changes form sub-parallel, gently-curved bands which are localised at the grain tips (Fig. 2ab). The trend of the bands vary along their length, and is different at each tip of the grain. Several late brittle fractures truncate bands and have sharp changes in orientation across them (Fig. 2a-b). EBSPs from different localities within the grain show subtle variations in the positions of bands and band intersections (zone axes) (Fig. 2c). These variations confirm that the greyscale differences in orientation contrast images correspond to changes in crystallographic orientation. Indexing of these EBSPs results in low MADs (Table 2) and indicates that there are no systematic pseudosymmetry misindexing problems associated with EBSD analysis of zircon.

Automatic orientation mapping shows that the zircon contains heterogeneously developed intragrain orientation variations (Fig. 3a) with maximum cumulative disorientation from the parent orientation in areas A, B and C of 14˚, 6˚ and 4˚ respectively (Fig. 3a). The total cumulative disorientation across the whole grain is *c.* 20˚. Disorientation profiles at the grain tips show a progressive change in crystallographic orientation (Fig. 3b). Correlated disorientation angle analysis from the data shown in Fig. 3a indicate that the magnitude of disorientation between adjacent points never exceeds 4˚ across the grain, and over 95% of adjacent points have a misorienation of <1˚ at 3µm grid spacing. Variations in crystallographic orientations across individual brittle fractures is *c.* 0.5˚ (Fig. 3b), and the accommodation of orientation variations at the grain scale by brittle deformation is insignificant (Fig. 3a). The orientation of the undeformed parts of the grain with respect to the sample surface is such that the zircon c-axis plunges gently to the upper right of the map (Fig. 3c).

The changes in crystallographic orientation across the grain are systematic and define cumulative dispersions away from the parent orientation that, in their simplest form, lie along small circles. In area A, the crystallographic axes are dispersed anticlockwise from the parent orientation along small circles about a ‘dispersion axis’ coincident with the (100) pole (Fig. 4ai). All disorientation axes for this area generally cluster in the vicinity of the same (100) pole, but 2-4˚ disorientations cluster more tightly than 1-2˚ and 0.5-1° disorientations (Fig. 4a ii). This may be a direct consequence of less accurate axis determination at low misorientation angles (Prior 1999). In areas B and C, the dispersion of crystallographic orientation from the undeformed core of the grain is more complex. Area B shows a ‘rhomb’ shaped dispersion pattern (Fig. 4bi) requiring dispersion of comparable magnitudes (<5°) around at least two axes. The 1-2º disorientation axes for area B also fail to correspond to a single crystallographic direction (Fig. 4bii) but define a girdle distribution parallel to the $(1\bar{1}0)$ plane. The dispersion pattern of crystallographic axes in area C also shows complexity associated with dispersion about multiple axes (Fig. 4ci). However these differ from those recorded in areas A and B. The geometries of disorientation axes are also different in area C with 2-4° axes being distributed around the $(1\bar{2}1)$ pole, while 1-2° axes are more scattered (Fig. 4cii). The small magnitudes of cumulative dispersion in the areas B & C make orientation analysis difficult. Therefore further detailed microstructural analysis is only applied to Area A.

The part of the grain with the largest cumulative disorientation (Area A) contains numerous discrete boundaries that separate zones (2-10μm wide) that record little internal orientation variation. (Fig. 5). These boundaries generally lie sub-parallel to each other (Fig 5a,b). Disorientation axes/angle analysis of various boundaries reveals some variability in the geometry of disorientation axes (Fig. 5c).This could reflect errors associated with the calculation of low-angle disorientation axes (Prior 1999). However, sub-areas 2,3, & 4 (Fig. 5a) record disorientation axes associated with 1-2° disorientation angles that plot close to the local (100) pole.

A numerical analysis of orientation correlations from area A (after Pantleon 2005), taking into account the tetragonal symmetry of zircon, indicates that the mean orientation of the zircon in this particular area is given by the quaternion, $\bar{q}$ = [0.82, -0.24, -0.52, 0.07]. Diagonalisation of the symmetric tensor $Q = \sum_i \delta\vec{q}_i \otimes \delta\vec{q}_i$, provides eigenvalues (λ) and eigenvectors ($\vec{r}$) which characterize the standard deviation of the orientation distribution within area A. Thus,

λ_1 = 0.06 with $\vec{r}_1 = [0.07 \quad 0.29 \quad 0.96]$

λ_2 = 0.19 with $\vec{r}_2 = [-0.09 \quad 0.95 \quad 0.29]$

λ_3 = 13.8 with $\vec{r}_3 = [0.99 \quad -0.11 \quad -0.04]$.

The orientation distribution with respect to the three principle axes $\delta\vec{q} = \delta q_1\vec{r}_1 + \delta q_2\vec{r}_2 + \delta q_3\vec{r}_3$ therefore indicates a dominant rotation axis parallel to $\vec{r}_3$ with only minor variations along other directions (Fig. 6a,b). This vector deviates only 6.5° from the crystallographic [100] direction. In map form these rotations around the dominant rotation axis indicate an underlying microstructure (Fig. 6c) similar to that shown in Fig. 5a and confirm the band-like changes in orientation across the grain.

The consistent change in orientation in Area A shown by the maps (Fig. 5a & 6c) and crystallographic orientation data (Fig. 4a) record an orientation gradient that is superimposed on the finer-scale orientation differences associated with the boundary structure (Fig. 7a). The effect of the orientaion gradient can be eliminated in the spatial direction (here [0.50, 0.87]) with the largest variation in sign carrying dislocation angle (Pantleon 2005) to show details of the boundary related microstructure (Fig 7b). The result is a decrease in orientation variation from 14° to 8° that can be shown in a modified disorientation map (Fig. 7c). This map illustrates that the boundary–related microstructure defines several domains. We have considered one of these domains and one of the domain boundaries in detail (shown in Fig. 8 & 9 respectively).

In domain (i), the detailed geometry of the boundaries is significantly more complex than can be recognised in Fig. 5a and comprises irregular kinked and smoothly curved boundaries (Fig. 8a-d). The magnitude of local disorientation associated with each boundary varies along its length and boundaries commonly terminate in broader domains of distributed strain (Fig. 8b,c). A disorientation profile (p-p') across the microstructure (Fig. 8b) indicates that the change is crystallographic orientation comprises areas recording no significant orientation variation interspersed with narrow zones which accommodate all of the cumulative disorientation (Fig. 8d).

In domain (ii) the change in crystallographic orientation is highly localised along single boundary planes (Fig. 9) and in such areas there is a dramatic reduction in EBSP band contrast (Fig. 9a). The width of these boundary zones are typically ~0.2µm (based on variations in band contrast) for changes in orientation of 0.5-3°. Disorientation axes from higher magnitude disorientation boundaries (sub-area ii; Fig 9b) record similar directions (Fig. 9d). A more detailed analysis of these domains is beyond the scope of this paper.

Discussion

Crystal Plastic Deformation of Zircon

The EBSD data from a zircon found within a deformed region of Indian Ocean crust indicate a progressive change in crystallographic orientation of 20°. This variation is localized at the grain tips, the core of the grain remaining undeformed, and corresponds to grain size reduction in the immediately adjacent matrix that is associated with dynamic recrystallization of plagioclase (Fig 1d). Microstructure developed in the zircon tips are characterized by abrupt boundaries that accommodate small (<3°) orientation changes within the lattice. These boundaries are of the order of 200 nm wide and are characterized by reduced band contrast. Between such boundaries, no systematic changes in orientation (>0.5°) are observed. In any particular grain tip the orientation variations associated with these boundaries are associated with rotations around one (Area A), two (Area B), or possibly more (Area C) axes. In addition, in the simpler system (Area A), the axis around which the crystallographic dispersion takes place is parallel to the disorientation axes relating adjacent EBSPs (Fig. 4). These axes coincide with the rational [100] crystallographic direction. These characteristics are consistent with the boundaries having formed by the migration and accumulation of dislocations into high dislocation density walls that separate relatively dislocation-free regions. The microstructure associated with changes in crystallographic orientation within the zircon is therefore interpreted to reflect crystal-plastic deformation rather than deformation by brittle fracture.

The relationship between localized deformation at the zircon tip and reduced plagioclase grain size in the immediately adjacent matrix indicates deformation of the zircon within the shear zone in which it currently resides. The nature of the type of deformation (coaxial vs non-coaxial shear) is difficult to resolve. However, the grain shape elongation of plagioclase at ~35° to the margin of the deformed zone is more consistent with a significant non-coaxial or simple shear component than formation by coaxial deformation. The localization of deformation to the zircon tips is therefore interpreted to reflect incompatibility between the deforming matrix and the zircon grain and a heterogeneous response to increased stress in the vicinity of the zircon tip - matrix interface (e.g. Ashby 1970; Kenkmann 2000) during localized non-coaxial deformation of the gabbro.

There are two end-member models commonly used to describe the relationship of dislocations and low-angle boundaries: the accumulation of edge dislocations into tilt boundaries (Fig 10a) and the formation of twist boundaries associated with screw dislocations (Fig 10b). Discrimination of these different boundary types and the recognition of slip systems responsible for their formation is possible using EBSD data. However, it generally requires the analysis of two sample sections to construct the three dimensional orientation of a particular boundary (Winther et al. 2004). In some situations, if ideal tilt or twist boundaries are assumed, the orientation of the dispersion / disorientation axes and the trace of the low-angle boundary on the sample surface provide information on boundary plane morphology in the third dimension without the necessity of multiple sections. In the case of low-angle tilt boundaries, the line of the dislocation lies parallel to the disorientation and crystallographic dispersion axes, lies within the plane of the low-angle boundary and is perpendicular to both the pole to the slip plane and the slip direction (Burgers vector) of the associated slip system (Fig. 10a,c,d). For twist boundaries, formed by two or more sets of screw dislocations, the rotation axis is perpendicular to the boundary plane (Fig. 10b). Although using simple geometric models, this approach has been successfully used in EBSD studies to determine dislocation slip systems in quartz (Lloyd et al. 1997), calcite (Bestmann and Prior 2003; Reddy and Buchan 2005), garnet (Prior et al. 2002) and pyrite (Boyle et al. 1998).

In the region recording the largest change in crystallographic orientation (Area A) the change in lattice orientation throughout the whole area corresponds to small circle dispersion around a single [100] direction pole (Fig. 4ai). Disorientation axes associated with this change in crystallographic orientation also lie parallel to the [100] direction (Fig. 4aii & Fig. 5) as does the direction of the calculated maximum rotational eigenvalue (Fig. 6) following a new approach to analyzing EBSD orientation data (Pantleon 2005). These observations, although representing different ways of analysing the same orientation data, indicate dominance of one rotation axis, [100], within area A (Fig. 5). This direction, along with the trace of the low-angle boundaries on the sample surface, can be used to determine the orientation of the low-angle boundaries (Fig 5). Since the (100) crystallographic plane and the trace of the low-angle boundaries on the sample surface do not coincide, the dominant microstructure is not consistent with a twist boundary geometry (Fig. 10). However, the data are consistent with a tilt boundary formed by edge dislocations with Burgers vector [001] and dislocation line

[100]. Such a boundary may be formed by migration and accumulation of dislocations of a [001] $(0\bar{1}0)$ glide system (Fig. 5). The relationship of this slip system to the atomic structure of zircon within an approximate sample coordinate system is illustrated in Fig. 11a.

The translational lattice repeat vector in the [001] direction is 0.5982 nm, the shortest in the zircon structure, and is significantly shorter than the Burgers vector (b) for <010>{100} slip (0.6607 nm; Table 2) identified in experimentally shocked zircon (Leroux et al. 1999). Commonly the energy of a dislocation is simply considered to be proportional to b^2 (e.g. Read 1953). The formation of dislocations associated with <001>{010} would therefore seem to be energetically more favourable than the experimentally verified <010>{100} system. However, in anisotropic materials the length of the Burgers vector can not be considered in isolation (Foreman 1955). In the case of zircon, the anisotropy in elastic properties (e.g. Sirdeshmukh and Subhadra 2005) must also be considered. If this is done (see Appendix 2), it can be shown that [001]c-type dislocations should be energetically favorable over the [010]a-type dislocations verified by TEM (Leroux et al. 1999). In addition, the zircon lattice is body centred ($I4/_{\mathrm{amd}}$) suggesting that the equal addition of two common dislocations with Burgers vectors ½$\langle 1\bar{1}1\rangle$ may be responsible for the apparent [001] c-type dislocations (Fig. 11b). EBSD data does not have the spatial resolution to be able to disciminate between these alternatives and such a possibility must be tested using TEM.

A similar disorientation analysis of the prominent boundary on the right side of area A (domain ii) yields a different result from those seen in the rest of Area A (Fig. 9). The surface trace of this boundary varies along its length but is ~70° from the general trend of other boundary traces in area A. The variation in crystallographic orientation across this 200nm wide boundary is 3° and is associated with a similar dispersion and disorientation axis geometry as the rest of Area A around [100]. The trace of this low-angle boundary is almost coincident with the (100) plane and is *c*.90° to the rotation axis, suggesting a twist boundary geometry consistent with screw dislocations of [100](100) and [001](100). However, the data are also consistent with tilt boundary formation associated with $[0\bar{1}0]$ (001). In reality, the trace of this particular boundary curves into the orientation of the [001] $(0\bar{1}0)$ tilt boundaries, and is likely to be composite boundary with an increasing component of [001] $(0\bar{1}0)$ slip with any of the above slip systems. A summary of the features shown in Area A is shown in Fig. 12.

The small variation in crystallographic orientation in area B makes possible slip systems, associated with low-angle boundary formation, difficult to identify. Low-angle boundaries in area B show curved traces (Fig. 2b) and crystallographic dispersion axes (Fig. 4bi) and disorientation axes (Fig. 4bii) show some variability lying on a single great circle corresponding to the $(1\bar{1}0)$ plane. If it is assumed that low-angle boundaries in Area B have a tilt geometry, cross slip associated with the same $[1\bar{1}0]$ glide direction could explain the great circle distribution of the disorientation axes. The disorientation axis distribution would then result from the activity of different slip planes, for example $(111), (11\bar{1})$ and (112). Such slip systems have not been previously reported in zircon and require verifying with TEM analysis.

In addition to the possibility of cross slip, there are alternative intepretations that must also be considered. Firstly, the variation in disorientation axis geometry could be due to errors associated with low-angle disorientation axis calculations (Prior 1999). It should be noted that the distributions of disorientation axes in area A (Fig. 4aii) show a statistical alignment to [100] that is also seen in the rotation axis associated with crystallographic dispersion and the orientation of maximum rotational eigenvalue obtained by the methodology of Pantleon (2005). This indicates that disorientation axes of <5° can be successfully used in microstructural analysis (cf. Prior 1999). It therefore seems unlikely that the systematic great circle distribution of the disorientation axes is associated with errors in the calculation of the disorientation axes in area B. Alternatively, a combination of different slip systems would result in disorientation axes that reflect a geometric mixing of more than one rotation. The boundary geometries seen in parts of area A (Fig. 8) and the complexities seen in numerical analysis of the orientation data (Fig. 7) indicate the necessity for complex interaction of other dislocations associated with less active slip systems. This is also recognized in the curved boundaries of Area B where there is no systematic spatial variation in disorientation axes geometry. Some of the disorientation axis data must therefore be interpreted to reflect a variable combination of more than one slip system; an interpretation that is supported by the complex patterns seen in crystallographic dispersion patterns (Fig. 4b). Although the complexity recorded here is reported at the µm-scale, similar complexity has recently been reported in dislocations at the nm-scale (Johnson et al 2004), showing it is a fundamental property of dislocation sub-structure.

In area C, the $[1\bar{2}1]$ disorientation axes (Fig. 4cii) correspond to boundary traces that define a number of different orientations. Combined with the observation that the dispersion of crystallographic axes does not reflect rotation around a single rotation axis (Fig. 4ci) but appears to be the product of a combination of slip systems, the interpretation of possible contributing slip systems is difficult without recourse to finer scale (TEM) studies.

Geometrically Necessary Dislocation Density

From the change in the crystallographic orientation, the geometrically necessary dislocation content (Cottrell 1964; Ashby 1970) can be obtained as the curvature of the crystalline lattice is directly associated with the dislocation density tensor (Nye 1953). Several methods have been proposed to resolve the type and density of the geometrically necessary dislocation content from the orientation changes evident from EBSD (Sun et al. 2000; El-Dasher et al. 2003). For cubic metals a severe complication arises as to the large number of possible slip system and the corresponding large number of dislocation types (characterized by Burgers vector and line vector) which has to be taken into account. This problem simplifies in the present case of zircon as only screw and edge dislocations with line and Burgers vectors along the elementary crystallographic axis [100], [010] and [001], in all nine dislocation types, must be considered. The determination of the individual dislocation densities will be addressed in a forthcoming paper. Here an estimation of the geometrically necessary dislocation content is based on the long range orientation gradient in area A. The curvature caused by an orientation change of 14° (0.244 radians) due to a slip system with Burgers vector, *b*, taking place over a distance of *c.*200 µm requires a dislocation density, $\rho = \Delta\theta/Lb = 2.10^{8}$ cm^{-2}. This is consistent with seven individual low-angle boundaries, spaced at *c.*30 µm and each having a disorientation angle of *c.*2° (0.035 radians), assuming their misorientation is mostly accumulative. Taking into account a width of each low-angle boundary of about 200 nm, the local dislocation density concentrated in such a boundary becomes 3.10^{10} cm^{-2}. This approach has some limitations, for example it ignores all dislocations associated with alternating disorientations. However, it provides a first approximation of dislocation densities associated with low-angle boundary formation in naturally deformed zircon.

Significance of Plastic Deformation Microstructures in Zircon

Although of low modal abundance, zircon is critical in controlling trace element distribution during high-grade metamorphism and melting, and also provides the means to date these processes through isotope geochronology. As a result there has been extensive research to understand the geochemical behaviour of zircon. Numerous empirical studies (e.g.Connelly

2000; Peck et al. 2003), experimental studies (Suzuki et al. 1992; Cherniak et al. 1997a; Cherniak et al. 1997b; Lee et al. 1997; Watson and Cherniak 1997; Cherniak and Watson 2001; Cherniak and Watson 2003) and numerical studies (Meis and Gale 1998) of elemental diffusion in zircon have shown that volume diffusion of most elements requires high-temperatures (>900°C) before significant elemental diffusion distances are achieved. This characteristic underpins the use of zircon in a wide range of geological environments to provide geochemical and temporal constraints on a range of different processes. Several studies in the past have demonstrated that zircon is capable of deforming by brittle fracture (Boullier 1980; Wayne and Sinha 1988; Steyrer and Sturm 2002); a mechanism that will modify the effective grain size and surface area of the zircon and therefore may have implications for diffusion and chemical reaction under certain crustal conditions. However, the observation reported here, that zircon may deform by the formation and migration of dislocations under crustal conditions, has some profound implications for the chemical behavior of zircon, in particular the modification of trace element composition and the assumption of isotopic closure below temperatures of 900°C, and the role of zircon in controlling trace element budgets during crustal melting.

The presence of intragrain microstructures (e.g. dislocations and low-angle boundaries) in crystalline material can significantly affect the bulk diffusion properties of that material (e.g. Lee 1995 and references therein). The reasons for this are several fold. The diffusion characteristics of dislocations are significantly different from the diffusion parameters associated with volume diffusion in a dislocation-free lattice. At any given temperature, diffusion along the line of the dislocation is characterized by orders of magnitude larger diffusion coefficients and significantly smaller activation energies than diffusion in the dislocation-free lattice (Balluffi 1970; Yund et al. 1981; Yund et al. 1989; Yurimoto et al. 1992; Li and Chou 1996). Diffusion properties within low-angle boundaries are such that they also lead to faster diffusion than in the pristine lattice (Klinger and Rabkin 1999), while there is also evidence for a direct relationship between changing diffusion parameters and misorientation in low- to high- angle boundaries (Ma and Balluffi 1993; Li and Chou 1996). This indicates that fast-diffusion pathways are far more complex than simple pipe-diffusion models associated with single sets of dislocations. Plastic deformation accommodated by the formation and migration of dislocations into low- and ultimately higher angle boundaries is therefore likely to produce multiple diffusion pathways that have different diffusion properties depending on the evolving microstructure.

In detail, the relative contributions of dislocation-related diffusion and volume diffusion to bulk diffusion characteristics of a material will vary because of the non-linear relationship between diffusion and temperature. As a result, the importance of high diffusivity pathways may change during the thermal evolution of a sample, with dislocation-related diffusion becoming more significant at lower temperatures because of the relatively high diffusion coefficient and low activation energy with respect to volume diffusion. This may have significant implications for the extrapolation of high temperature experimental volume diffusion studies to lower temperatures where dislocation-related diffusion would become relatively more significant. In addition it would be expected that for zircon in which recrystallization following radiation damage is negligible, changes in zircon geochemistry, for example Pb loss (Gebauer and Grünenfelder 1976) or REE modification (Reddy et al. 2006), will reflect the dominance of the dislocation-related diffusion process under most crustal conditions.

Although microstructures can modify the diffusion characteristics of a material, the impact of dislocations and low-angle boundaries on bulk diffusion characteristics of the material will depend upon the total number and geometry of the high diffusivity pathways and whether the diffusing material have a propensity to be located in the high diffusivity defect (Lee 1995; Klinger and Rabkin 1999). In strongly deformed materials with high dislocation densities, volume diffusion distances between fast diffusion pathways are considerably reduced, leading to enhanced bulk diffusion. In addition, the mobility of high diffusivity pathways, once formed, plays a critical role in the extent to which the chemistry of the deforming material may be modified. In the case where dislocations are migrating during the formation of low-angle boundaries (Fig. 10a), the surrounding volume of material is swept by migrating dislocations, resulting in transient fast diffusion pathways that have the ability to interact with a greater volume of crystalline material (Ruoff and Balluffi 1963). The effect of dislocation migration will be further enhanced if the partition coefficient of the diffusing species into dislocations >>1 (Lee 1995), as would be the case for Pb in zircon.

A characteristic of chemical changes associated with dislocation migration and low-angle boundary formation is that the relatively dislocation-free volumes between low-angle boundaries should also be chemically modified. This seems to be the case in REE variations in area A of the studied zircon, where diffusion distances approach five orders of magnitude those calculated for volume diffusion (Reddy et al. 2006). These data therefore provide the empirical evidence that enhanced bulk diffusion associated with high-diffusivity pathways and defect-related diffusion can modify zircon geochemistry at temperatures below those predicted by volume diffusion experiments.

Solid-state diffusion in zircon is an important control on the trace element geochemistry of Zr saturated melts (Watson and Harrison 1983). While in Zr undersaturated melts, the dissolution and solubility of zircon has a critical role in controlling trace element geochemistry (Watson and Harrison 1983; Baker et al. 2002). The presence of high dislocation densities associated with plastic deformation has the potential to affect trace element geochemistry of melts, firstly, as outlined above, by enhancing bulk diffusion in zircon and secondly by modifying the zircon dissolution characteristics. Research on the dissolution of silicate minerals (Wintsch 1985; Wintsch and Dunning 1985; Blum et al. 1990), carbonates (Morse and Arvidson 2002) and halite (Bosworth 1981) all indicate enhanced, though non-linear, dissolution in the presence of crystal defects such as dislocations. This enhanced dissolution reflects both higher dissolution rates associated with increased internal energy of dislocations, and enhanced nucleation of dissolution pits where dislocations intersect the crystal surface. Dislocation densities required to significantly modify internal energies of silicates are *c.*10^9 cm^{-2} (Wintsch and Dunning 1985). Although the bulk dislocation density in area A is less than this, the low-angle boundaries have dislocation densities that are an order of magnitude greater than this ($\sim 10^{10} cm^{-2}$). Dislocation densities of this magnitude also have the potential to significantly enhance silicate dissolution in metamorphic environments approaching equilibrium (Blum et al. 1990). Consequently, the dissolution characteristics of zircon can potentially be modified by the presence of crystal-plastic deformation microstructures and this could increase metamorphic reaction kinetics and significantly affect the trace element budget of silicate melts.

To date, the full range of conditions under which zircon can deform by crystal-plastic processes have not been constrained. In this study, plastic deformation via <001>{010}, and <010>{001} edge or <100>{100) and <001>{100} screw dislocations , plus <010> cross slip on took place under amphibolite facies conditions. Amphibolite facies and higher grade metamorphic rocks are often intensely deformed and comprise a large percentage of the Earth’s outcropping basement. Preliminary microstructural analyses of zircon collected from a number of different high-grade localities indicate that, although not affecting all grains, microstructures developed during plastic deformation are present in all of the analyzed samples. A preliminary study of 200 randomly sampled Jack Hills zircons indicates that *c.*5% of the analyzed zircon grains contain deformation-related low-angle boundaries (Timms et al., unpublished data). Although 5% may not seem significant, it is important to recognize that many of the recent applications of zircon geochemistry to the understanding of ancient geological environments involve the high spatial resolution analysis of small numbers of zircon grains and in all cases, microstructural analysis of the samples has not been undertaken.

An important aspect of the microstructural results presented here is the scale of deformation microstructures relative to popular geochemical/geochronological analysis techniques. Natural zircon grain populations used for geochronology are typically smaller than the grain analyzed in this study, and are more likely to be of similar volume as area A. This highlights that plastic deformation can affect significant volumes of natural zircon grains. Further, deformation microstructure can have very subtle effects on the zoning observed in panchromatic cathodoluminescence imaging (Reddy et al. 2006), and could easily be overlooked. Geochemical analyses of zircon are increasingly concentrating on smaller volumes of material. Current ion-probe technologies typically analyze 20μm diameter pits which would cover a range of different deformation sub-structures with potentially different geochemical characteristics in a deformed zircon (Fig. 9a). Clearly this could lead to erroneous and misleading interpretations of ion probe data unless deformation microstructures are identified. The best approach for this identification is a rapid investigation of *in situ* or mounted zircon using orientation contrast imaging on samples used to characterize compositional variations by CL imaging. Microstructures identified at this reconnaissance stage can then be further analyzed using quantitative EBSD analysis.

It is widely accepted that the crystallization and dissolution of zircon, and its chemical modification through diffusion, is dependent upon factors such as grain size, temperature, bulk-rock (or melt) composition, and the operation of metamorphic reactions. However, the importance of crystal plastic deformation of zircon has largely been ignored. The recognition of orientation variations in zircon associated with crystal-plastic deformation and the recognition that associated microstructures can facilitate modification of zircon geochemical systems is a possible explanation for anomalous geochemical and isotopic data that could ultimately be developed to provide new geological applications; for example the dating of deformation. Importantly, the ability of deformation-related microstructures to act as fast-diffusion pathways that can significantly modify mineral trace and isotope geochemistry precludes the *a priori* use of volume diffusion models to interpret zircon trace element and isotope data without first characterizing zircon microstructure. In addition, assumptions about the dissolution characteristics of zircon during crustal melting should also be reexamined to establish the possible significance of deformation-related microstructures.

Figure Captions

Fig.1. a) Location of the Atlantis II Fracture Zone and Hole 735B (after Bach et al. 2001). b) Optical plane-polarized photomicrograph showing the single zircon grain used in this study in a high strain zone with a fine grained recrystallized matrix of plagioclase, magnetite, ilmenite and pyroxene between two large primary orthopyroxene (OPX) and plagioclase (plag) grains. c) map derived from EBSD data showing the distribution of phases in the high strain zone. d) map showing the size distribution of plagioclase grains. Plagioclase grains are shaded on a gradational color scale according to their area and are superimposed over a grey-scale band contrast map. Note the bands of smaller plagioclase grains (blue) localized at the tips of the zircon grain.

Fig. 2 a) Orientation contrast image of the zircon grain. Grey-scale variations within the zircon grain indicate qualitative variations in crystallographic orientation. Box indicates area shown in (b). b) Orientation contrast image showing the detail of a deformed area of the zircon grain. c) A series of EBSPs from numbered spots shown in (a) illustrating the change in crystallographic orientation associated with grey-scale variations in (a). A grid has been added to aid visual comparison between EBSPs.

Fig. 3 a) Orientation map of the single zircon grain obtained by automatic EBSD mapping. Each pixel corresponds to the analysis of a single EBSP. Colors indicate a relative minimum change in crystallographic orientation (disorientation) from reference point "+" (blue) to a maximum of 14° (red). Non-zircon points are shaded for band contrast (grayscale) to depict matrix grain structure. Boxes indicate areas from which crystallographic information are reported. Note that the brittle fractures seen in Fig. 2a have no significant impact on orientation variations at the grain scale. b) Cumulative disorientation profiles for lines a-a', b-b' and c-c' in (a). c) Lower hemisphere equal area projection of low index directions of zircon for the reference point '+' shown in (a). Pole data is represented in the sample reference frame (x-y) and have been assigned specific directions to facilitate description and interpretation.

Fig. 4. Crystallographic orientation and disorientation data for (a) sub-area A, (b) sub-area B, and (c) sub-area C shown in Fig. 3a. i) Lower hemisphere equal area pole figure of each data point in the sub-area. Colors correspond to disorientation from reference orientation as shown in Fig. 3a. Inset is an enlargement of a pole to (111) to show the dispersion in detail. Dispersion corresponds to small circle rotations of crystallographic axes around [100]. ii) Lower hemisphere equal area projection of low-angle disorientation axes (0.5-4°) plotted in the sample reference frame. Grey symbols correspond to low-index crystallographic axes shown in Fig. 3c.

Fig.5. a) Orientation map of Area A shown in Fig. 3a obtained by automated EBSD mapping at 1μm spacing. Map is colored for disorientation angle (up to 14°) from a reference point indicated by a cross in the lower left. Non-zircon points are shaded for band contrast to illustrate matrix grain structure. Boundaries above 0.5° are shown. White boxes delimit subsets of disorientation axes data shown in (c). Areas (i) and (ii) are shown in Figs 8 and 9. b) Map derived from EBSD data that shows the small orientation changes (or 'local disorientation') between pixels, highlighting regions of higher deformation. Every pixel shows the mean disorientation angle between that pixel and its 8 surrounding pixels. c) Disorientation axes data from subareas shown in (a). Lower hemisphere equal area plots show 0.5-4° disorientation axes, boundary trace orientation (shown as thick black line outside primitive circle), and crystallographic poles of the reference orientation (grey symbols; for legend see Fig. 3c). To aid interpretation of the data (see discussion), the inferred great circle for the boundary wall (red) and slip plane (green) have been added assuming a tilt boundary geometry where the [100] disorientation axis correlates with the line of the dislocation vector. In this scenario, the pole to the boundary wall [001] corresponds to the orientation of the Burgers vector.

Fig. 6. Disorientation of the individual orientation data points with respect to the average orientation in "disorientation space" for Area A. a) shows a cigar shaped distribution with respect to calculated eigenvector orientations. b) indicates a projection of disorientation space onto two of the principal axes (δq_1 and δq_3). Colors show positive (blue) and negative (red) rotations from the average orientation in Area A. c) Map of orientation data colored (as in b). Disorientations corresponding to rotations purely around directions orthogonal to $\vec{r}_3$ (i.e., having no component along $\vec{r}_3$) appear white.

Fig. 7. a) Graph to show sign carrying disorientation angle (θ^*) with distance (x^*) along the direction of maximum curvature in Area A. Definition of θ^* (inset) is after Pantleon, (2005). Black line indicates a cubic parabola that represents a 1st order variation in the orientation of the crystal lattice. Subtraction of this parabola effectively removes the bending component in the grain and enables detail of the local disorientation microstructure to be investigated (b). Replotting the disorientations around the dominant rotation axis ($\vec{r}_3$) after subtraction of the overall gradient (and enhancement of the color scale by a factor of 3) results in the map shown in c) (red = -2°, white = 0°, red = 2°). Dashed lines on the map correspond to microstructural domain boundaries that are defined by the gradient-subtracted microstructure shown in the direction of maximum curvature in (b). White boxes labeled (i) and (ii) correspond to analyses of one of these domains (Fig. 8) and a domain boundary (Fig. 9) respectively.

Fig. 8 Detailed maps of the deformed tip of the grain derived from EBSD data (area (i); Fig. 7). a) EBSP band contrast map. Domains of different band contrast values correspond to slight changes in orientation. Note the localized sharp reduction in band contrast along low-angle boundaries. Dashed circles indicate positions of SHRIMP analyses from Reddy et al. (2006). b) Map showing orientation changes relative to reference point (white cross). Color scale varies from 0° (blue) to 6° (red). c) Local disorientation map. For each pixel, the minimum misorientation magnitude is calculated for adjacent pixels on a local 3x3 grid, and the mean disorientation value is represented on the map. Narrow linear 'high-value' domains (low-angle boundaries) are commonly joined by broader domains (relay zones) of more distributed deformation. d) Cumulative disorientation profile (p-p’) in (b). The step type geometry indicates that much of the orientation variation is localized in discrete low-angle boundaries, with areas between these boundaries showing little orientation variation. Note that these maps are rotated with respect to sample coordinates (xy).

Fig. 9 a) EBSP band contrast, b) disorientation and boundary, and c) local disorientation maps of area (ii) in Fig. 7 showing the structure of a low-angle boundary. d) Lower hemisphere, equal area projection of the disorientation axes (>1˚) associated with the boundary shown in (a)-(c). Data fall close to [100]. Grey symbols show the crystallographic reference point shown by the white cross in (b). Black lines shown at the edge of the stereonet (NE & SW) correspond to the approximate trace of the boundary.

Fig. 10. Schematic representation of a) symmetric low-angle tilt boundary and b) twist boundary showing the geometric relationships between the boundary wall, slip plane, slip direction, and rotation axis and dispersion angle due to dislocation glide. c) Stereographic projection of the boundary/slip system shown in (a). At low tilt magnitudes the slip plane, slip direction and rotation axis are mutually perpendicular, and the rotation axis and pole to slip plane are contained within the plane of the boundary wall. d) Stereographic projection showing the dispersion of linear features A and B along small circles around the rotation axis.

Fig 11. Atomic models of zircon showing zirconium (blue), silicon (pink) and oxygen (red) positions and different possible zircon slip systems. a) slip system $[001]\left(0\bar{1}0\right)$ inferred from analysis of the EBSD from Area A. The crystal axes (ac) are oriented to show the alignment of lattice planes and glide directions within the approximate sample coordinate system (xyz). b) Possible $\frac{1}{2}\langle 1\bar{1}1\rangle$ Burgers vectors associated with dislocations in body-centered tetragonal zircon. Addition of two such dislocations would be equivalent to the [001]c Burgers vector shown in (a). a) & b) were created using the GDIS crystal program (Fleming and Rohl 2005).

Fig. 12. Block diagram illustrating low-angle boundary geometry and the slip system geometries in area A of the deformed zircon with respect to orientation variations shown in Fig. 5.

Table 1. Summary of previous microstructural features recorded in zircon.

Table 2. SEM Settings and EBSD collection and processing variables.

Table 3. Zircon crystallographic data (Mincryst Card #5260 after data of Hazen & Finger, 1979) used to generate the theoretical EBSD reflector files by which empirically obtained EBSPs are indexed.

References

Ashby MF (1970) The deformation of plastically non-homogenous materials. Philosophical Magazine 21:399-424

Bach W, Humphris SE, Erzinger J, Dick HJB, Alt JC, Niu Y (2001) The geochemical consequences of late-stage low-grade alteration of lower ocean crust at the SW Indian Ridge: Results from ODP Hole 735B (Leg 176). Geochim. Cosmochim. Acta 65:3267-3287

Baker DR, Conte AM, Freda C, Ottolini L (2002) The effect of halogens on Zr diffusion and zircon dissolution in hydrous metaluminous granitic melts. Contrib. Mineral. Petrol. 142:666-678

Balluffi RW (1970) On measurements of self-diffusion rates along dislocations in F.C.C. metals. Phys. stat. sol. 42:11-34

Belousova EA, Griffen WL, O'Reilly SY, Fisher NI (2002) Igneous zircon: trace element composition as an indicator of source rock type. Contrib. Mineral. Petrol. 143:602-622

Bestmann M, Prior DJ (2003) Intragranular dynamic recrystallisation in naturally deformed calcite marble: diffusion accommodated grain boundary sliding as a result of subgrain rotation recrystallization. J. Struct. Geol. 25:1597-1613

Bhimasenachar J, Venkataratnam G (1955) Elastic constants of zircon. The Journal of the Acoustical Society of America 27:922

Blum AE, Yund RA, Lasaga AC (1990) The effect of dislocation density on the dissolution rate of quartz. Geochim. Cosmochim. Acta 54:283-297

Bosworth W (1981) Strain-induced preferential dissolution of halite. Tectonophysics 78:509-525

Boullier AM (1980) A preliminary study on the behaviour of brittle minerals in a ductile matrix: example of zircons and feldspars. J. Struct. Geol. 2:211-217

Boyle AP, Prior DJ, Banham MH, Timms NE (1998) Plastic deformation of metamorphic pyrite: new evidence from electron backscatter diffraction and forescatter orientation-contrast imaging. Miner. Deposita 34:71-81

Cawood PA, Sircombe K, Nemchin AA, Freeman M (2003) Linking source and sedimentary basin: Detrital zircon record of sediment flux along a modern river system and implications for provenance studies. Earth Planet. Sci. Lett. 210:259-268

Cherniak DJ, Hanchar JM, Watson, E.B. (1997a) Rare-earth diffusion in zircon. Chem. Geol. 134:289-301

Cherniak DJ, Hanchar JM, Watson EB (1997b) Diffusion of tetravalent cations in zircon. Contrib. Mineral. Petrol. 127:383-390

Cherniak DJ, Watson EB (2001) Pb diffusion in zircon. Chem. Geol. 172:5-24

Cherniak DJ, Watson EB (2003) Diffusion in zircon. In: Hanchar JM, Hoskin PWO (eds) Zircon. Reviews in Mineralogy and Geochemistry, v. 53. Mineralogical Society of America, Washington, pp 113-143

Chichagov AV, Varlamov DA, Dilanyan RA, Dokina TN, Drozhzhina NA, Samokhvalova OL, Ushakovskaya TV (2001) MINCRYST: a Crystallographic Database for Minerals, Local and Network (WWW) Versions. Crystallography Reports 46:876-879

Collins AS, Reddy SM, Buchan C, Mruma A (2004) Temporal constraints on Palaeoproterozoic eclogite formation and exhumation (Usagaran Orogen, Tanzania). Earth Planet. Sci. Lett. 224:175-192

Connelly JN (2000) Degree of preservation of igneous zonation in zircon as a signpost for concordancy in U/Pb geochronology. Chem. Geol. 172:25-39

Cottrell AH (1964) The Mechanical Properties of Matter, Wiley, New York, p 223

DeCelles PG, Gehrels GE, Quade J, LaReau B, Spurlin M (2000) Tectonic Implications of U-Pb Zircon Ages of the Himalayan Orogenic Belt in Nepal. Science 288:497-499

Dempster TJ, Hay DC, Bluck BJ (2004) Zircon growth in slate. Geology 32:221-224

Dick HJB, Bach W, Bideau D, Gee JS, Haggas S, Hertogen JGH, Hirth G, Holm PM, Ildefonse B, Iturrino GJ, John BE, Kelley DS, Kikawa E, Kingdon A, LeRoux PJ, Maeda J, Meyer PS, Miller DJ, Naslund HR, Niu YL, Robinson PT, Snow J, Stephen RA, Trimby PW, Worm HU, Yoshinobu A, Natland JH, Alt JC (2000) A long in situ section of the lower ocean crust: Results of ODP Leg 176 drilling at the Southwest Indian Ridge. Earth Planet. Sci. Lett. 179:31-51

El-Dasher BS, Adams BL, Rollett AD (2003) Viewpoint: experimental recovery of geometrically necessary dislocation density in polycrystals. Scripta Materialia 48:141-145

Fitzsimons ICW, Kinny PD, Harley SL (1997) Two stages of zircon and monazite growth in anatectic leucogneiss: SHRIMP constraints on the duration and intensity of Pan-African metamorphism in Prydz Bay, East Antarctica. Terra Nova 9:47-51

Fleming S, Rohl AL (2005) GDIS: a visualization program for molecular and periodic systems. Zeitschrift für Kristallographie 220:580-584

Foreman AJE (1955) Dislocation energies in anisotropic crystals. Acta Metallurgica 3:322-330

Gebauer D, Grünenfelder M (1976) U-Pb zircon and Rb-Sr whole-rock dating of low grade metasediments. Example: Montagne Noire (Southern France). Contrib. Mineral. Petrol. 59:13-32

Geisler T (2002) Isothermal annealing of partially metamict zircon: evidence for a three-stage recovery process. Phys. Chem. Miner. 29:420-429

Geisler T, Kurtz R, Pidgeon RT, van Bronswijk W (2002) Transport of uranium, thorium, and lead in metamict zircon under low-temperature hydrothermal conditions. Chem. Geol. 191:141-154

Grimmer H (1980) A unique description of the relative orientation of neighbouring grains. Acta Crystallography A36:382-389

Gulson BL, Krogh TE (1973) Old lead components in the young Bergell Massif, south-east Swiss Alps. Contrib. Mineral. Petrol. 40:239-252

Hawkesworth CJ, Kemp AIS (2006) Using hafnium and oxygen isotopes in zircons to unravel the record of crustal evolution. Chem. Geol. 226:144-162

Hazen RM, Finger LW (1979) Crystal structure and compressibility of zircon at high pressure. Am. Mineral. 64:196-201

Hoskin PWO, Ireland TR (2000) Rare earth element chemistry of zircon and its use as a provenance indicator. Geology 28:627-630

Hoskin PWO, Schaltegger U (2003) The composition of zircon and igneous and metamorphic petrogenesis. In: Hanchar JM, Hoskin PWO (eds) Zircon. Reviews in Mineralogy and Geochemistry, v. 53. pp 27-62

Humphreys FJ, Bate PS, Hurley PJ (2001) Orientation averaging of electron backscattered diffraction data. J. Microsc. 201:50-58

John BE, Foster DA, Murphy JM, Cheadle MJ, Baines AG, Fanning CM, Copeland P (2004) Determining the cooling history of in situ lower oceanic crust - Atlantis Bank, SW Indian Ridge. Earth Planet. Sci. Lett. 222:145-160

Kenkmann T (2000) Processes controlling the shrinkage of porphyroclasts in gabbroic shear zones. J. Struct. Geol. 22:471-487

Klinger L, Rabkin E (1999) Beyond the Fisher model of grain boundary diffusion: effect of structural inhomogeneity in the bulk. Acta Mater. 47:725-734

Lanyon R, Black LP, Seitz HM (1993) U-Pb zircon dating of mafic dykes and its application to the Proterozoic geological history of the Vestfold Hills, East Antarctica. Contrib. Mineral. Petrol. 115:184-203

Lee JKW (1995) Multipath diffusion in geochronology. Contrib. Mineral. Petrol. 120:60-82

Lee JKW, Williams IS, Ellis DJ (1997) Pb, U and Th diffusion in natural zircon. Nature 390:159-161

Leroux H, Reimold WU, Koeberl C, Hornemann U, Doukhan JC (1999) Experimental shock deformation in zircon: a transmission electron microscopic study. Earth Planet. Sci. Lett. 169:291-301

Li XM, Chou YT (1996) Low angle grain boundary diffusion of Cr in Nb bicrystals. Philosophical Magazine A: Physics of Condensed Matter, Structure, Defects and Mechanical Properties 73:1303-1311

Lloyd GE, Farmer AB, Mainprice D (1997) Misoreintation analysis and the formation and orientation of subgrain and grain boundaries. Tectonophysics 279:55-78

Lloyd GE, Freeman B (1994) Dynamic recrystallization of quartz under greenschist facies conditions. J. Struct. Geol. 16:867-881

Ma Q, Balluffi RW (1993) Diffusion along [001] tilt boundaries in the Au/Ag system. I. Experimental results. Acta Metallurgia et Materialia 41:133-144

Meis C, Gale JD (1998) Computatonal study of tetravalent uranium and plutonium lattice diffusion in zircon. Mater. Sci. Eng. B57:52-61

Mezger K, Krogstad EJ (1997) Interpretation of discordant U-Pb zircon ages: an evaluation. J. Metamorph. Geol. 15:127-140

Mojzsis SJ, Harrison TM, Pidgeon RT (2001) Oxygen-isotope evidence from ancient zircons for liquid water at the Earth's surface 4300 Myr ago. Nature 409:178-181

Morawiec A (2003) Orientations and Rotations: Computations in Crystallographic Textures, Springer-Verlag, Berlin, p 210

Morse JW, Arvidson RS (2002) The dissolution kinetics of major sedimentary carbonate minerals. Earth Science Reviews 58:51-84

Nye JF (1953) Some geometric relations in dislocated crystals. Acta Metallurgica 1:153-162

Ozkan H, Cartz L, Jamieson JC (1974) Elastic constants of nonmetamict zirconium silicate. J. Appl. Phys. 45:556-562

Pankhurst RJ, Pidgeon RT (1976) Inherited isotope systems and the source region pre-history of early Caledonian granites in the Dalradian Series of Scotland. Earth Planet. Sci. Lett. 31:55-68

Pantleon W (2005) Retrieving orientation correlations in deformation structures from orientation maps. Materials Science and Technology 21:1382-1396

Peck WH, Valley JW, Graham CM (2003) Slow oxygen diffusion rates in igneous zircons from metamorphic rocks. Am. Mineral. 88:1003-1014

Pidgeon RT, Compston W (1992) A SHRIMP ion probe study of inherited and magmatic zircons from four Scottish Caledonian granites. Trans. R. Soc. Edinburgh: Earth Sci. 83:473-483

Prior DJ (1999) Problems in determining the misorientation axes, for small angular misorientations, using electron backscatter diffraction in the SEM. J. Microsc. 195:217-225

Prior DJ, Boyle AP, Brenker F, Cheadle MC, Day A, Lopez G, Peruzzo L, Potts GJ, Reddy S, Spiess R, Timms NE, Trimby P, Wheeler J, Zetterström L (1999) The application of electron backscatter diffraction and orientation contrast imaging in the SEM to textural problems in rocks. Am. Mineral. 84:1741-1759

Prior DJ, Trimby PW, Weber UD, Dingley DJ (1996) Orientation contrast imaging of microstructures in rocks using forescatter detectors in the scanning electron microscope. Mineral. Mag. 60:859-869

Prior DJ, Wheeler J, Peruzzo L, Spiess R, Storey C (2002) Some garnet microstructures: an illustration of the potential of orientation maps and misorientation analysis in microstructural studies. J. Struct. Geol. 24:999-1011

Read WT (1953) Dislocations in Crystals, McGraw Hill Ltd, London, p 228

Reddy SM, Buchan C (2005) Constraining kinematic rotation axes in high-strain zones: a potential microstructural method? In: Gapais D, Brun JP, Cobbold PR (eds) Deformation Mechanisms, Rheology and Tectonics: From Minerals to the Lithosphere. Geological Society Special Publication, 243. pp 1-10

Reddy SM, Timms NE, Trimby P, Kinny PD, Buchan C, Blake K (2006) Crystal-plastic deformation of zircon: A defect in the assumption of chemical robustness. Geology 34:257-260

Rhyzova TV, S. AK, Korobhova VM (1966) The elastic properties of rock-forming minerals V: additional data on sillicates. Izv. Earth Phys. 2:63

Ross GM, Parrish RR, Winston D (1992) Provenance and U---Pb geochronology of the Mesoproterozoic Belt Supergroup (northwestern United States): implications for age of deposition and pre-Panthalassa plate reconstructions. Earth Planet. Sci. Lett. 113:57-76

Rubatto D, Hermann J (2003) Zircon formation during fluid circulation in eclogites (Monviso, Western Alps): Implications for Zr and Hf budget in subduction zones. Geochim. Cosmochim. Acta 67:2173-2187

Rubatto D, Williams IS, Buick IS (2001) Zircon and monazite response to prograde metamorphism in the Reynolds Range, central Australia Contrib. Mineral. Petrol. 140:458-468

Ruoff AL, Balluffi RW (1963) Strain-enhanced diffusion in metals. II. Dislocation and grain-boundary short ciruiting models. J. Appl. Phys. 34:1848-1853

Schaltegger U, Fanning CM, Gunther D, Maurin JC, Schulmann K, Gebauer D (1999) Growth, annealing and recrystallization of zircon and preservation of monazite in high-grade metamorphism: conventional and in-situ U-Pb isotope, cathodoluminescence and microchemical evidence. Contrib. Mineral. Petrol. 134:186-201

Schwartz AJ, Kumar M, Adams BL (2000) Electron Backscatter Diffraction in Materials Science, Kluwer Academic / Plenum Publishers, New York, p 339

Schwartz JJ, John BE, Cheadle MJ, Miranda EA, Grimes CB, Wooden JL, Dick HJB (2005) Dating the Growth of Oceanic Crust at a Slow-Spreading Ridge. Science 310:654-657

Silver LT (1964) The relation between radioactivity and discordance in zircons. National Research Council Publication 1075:34-39

Sirdeshmukh DB, Subhadra KG (2005) Review: Consistency checks on elastic properties of crystals. Journal of Materials Science 40:1553-1570

Steyrer HP, Sturm R (2002) Stability of zircon in a low-grade ultramylonite and its utility for chemical mass balancing: The shear zone at Miéville, Switzerland. Chem. Geol. 187:1-19

Sun S, Adams BL, King WE (2000) Observations of lattice curvature near the interface of a deformed aluminum bicrystal. Philosophical Magazine 80:9-25

Suzuki K, Kouta H, Nagasawa H (1992) Hf-Zr interdiffusion in single crystal zircon. Geochem. J. 26:99-104

Valley JW (2003) Oxygen isotopes in zircon. In: Hanchar JM, Hoskin PWO (eds) Zircon. Reviews in Mineralogy and Geochemistry, v. 53. Mineralogical Society of America, Washington, pp 343-385

Watson EB, Cherniak DJ (1997) Oxygen diffusion in zircon. Earth Planet. Sci. Lett. 148:527-544

Watson EB, Harrison TM (1983) Zircon saturation revisited: temperature and composition effects in a variety of crustal magma types. Earth Planet. Sci. Lett. 64:295-304

Watson EB, Harrison TM (2005) Zircon thermometer reveals minimum melting conditions on earliest Earth. Science 308:841-844

Wayne DM, Sinha K (1988) Physical and chemical response of zircons to deformation. Contrib. Mineral. Petrol. 98:109-121

Whitehouse MJ, Platt JP (2003) Dating high-grade metamorphism - constraints from rare-earth elements in zircon and garnet. Contrib. Mineral. Petrol. 145:61-74

Wilde SA, Valley JW, Peck WH, Graham CM (2001) Evidence from detrital zircons for the existence of continental crust and oceans on the Earth 4.4 Gyr ago. Nature 409:175-178

Winther G, Huang X, Godfrey A, Hansen N (2004) Critical comparison of dislocation boundary alignment studied by TEM and EBSD: technical issues and theoretical consequences. Acta Mater. 52:4437-4446

Wintsch RP (1985) The possible effects of deformation on chemical processes in metamorphic fault zones., pp 251-268

Wintsch RP, Dunning J (1985) The effect of dislocation density on the aqueous solubility of quartz and some geologic implications: A theoretical approach. J. Geophys. Res. 90:3649-3658

Yund RA, Quigley J, Tullis J (1989) The effect of dislocations on bulk diffusion in feldspars during metamorphism. J. Metamorph. Geol. 7:337-341

Yund RA, Smith BM, Tullis J (1981) Dislocation-assisted diffusion of oxygen in albite. Phys. Chem. Miner. 7:185-189

Yurimoto H, Morioka M, Nagakawa K (1992) Oxygen self-diffusion along high diffusivity paths in forsterite. Geochem. J. 26:181-188

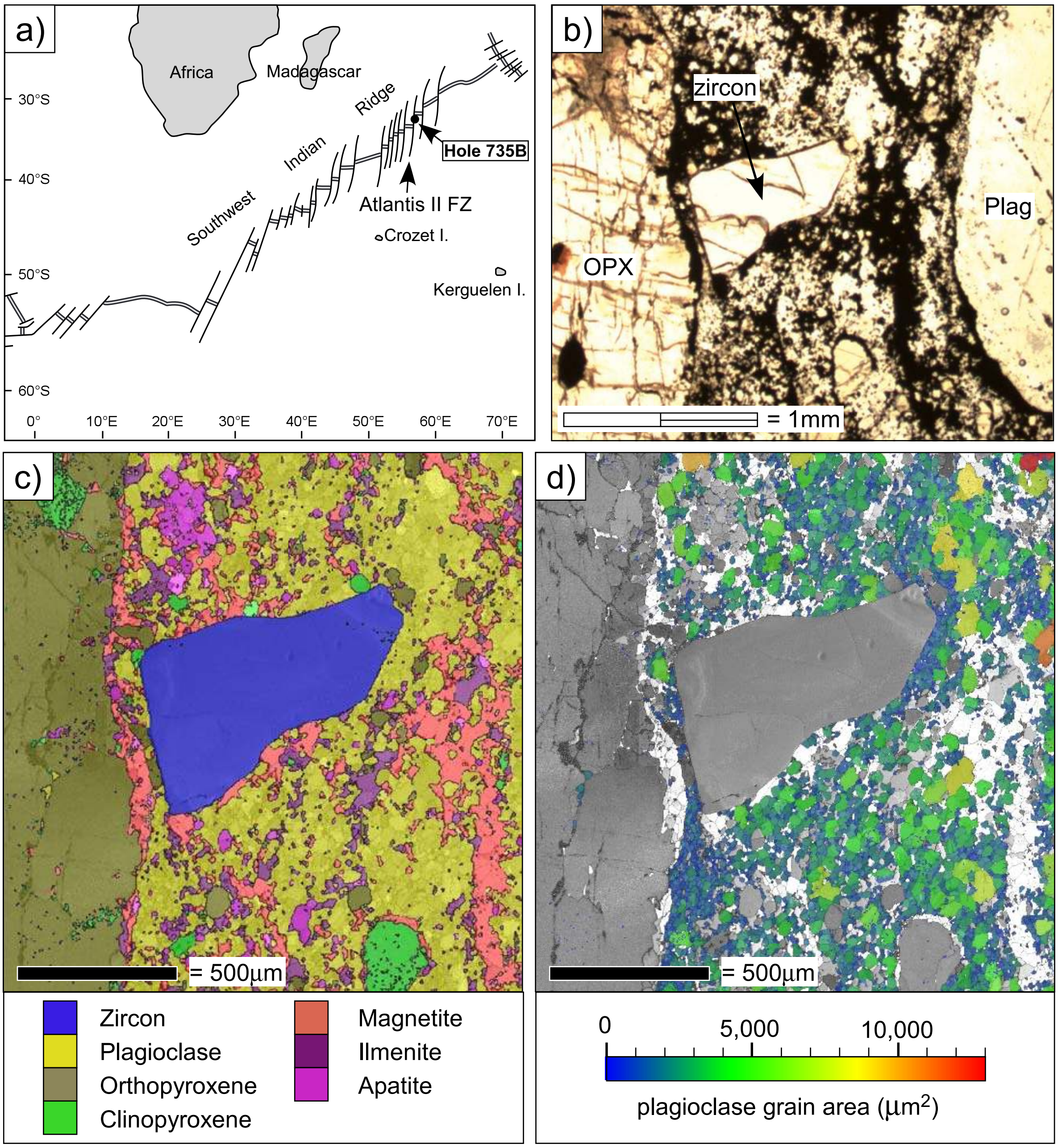

Reddy et al. / Zircon microstructure Figure 1

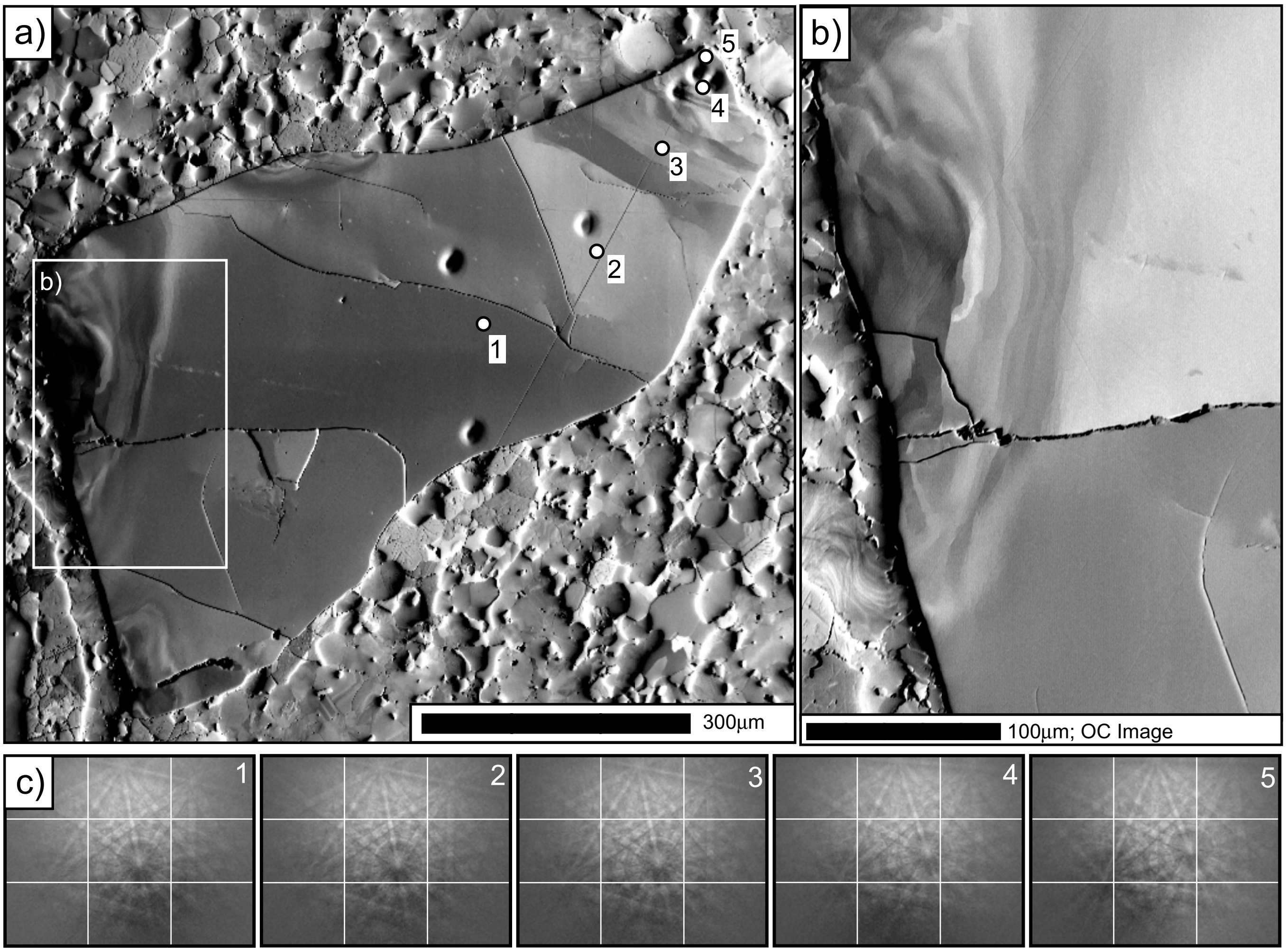

Reddy et al. / Zircon microstructure Figure 2

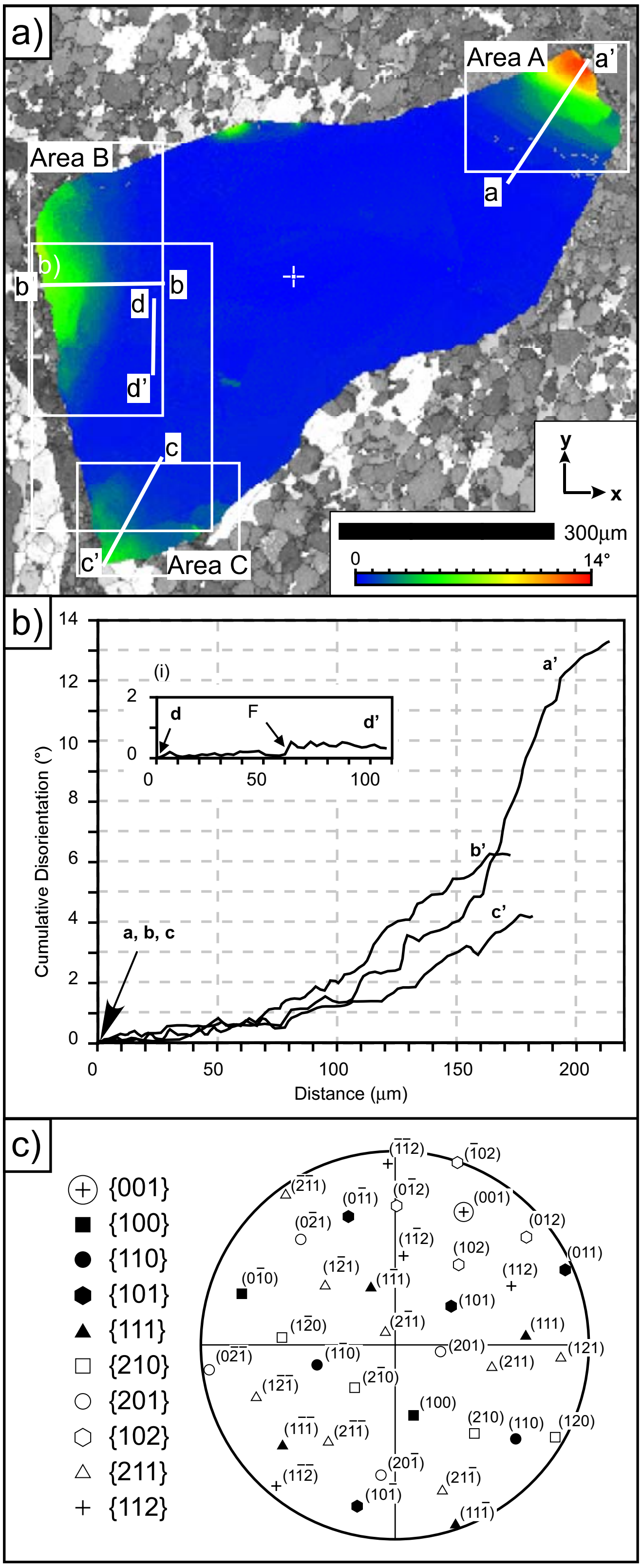

Reddy et al. / Zircon microstructure Figure 3

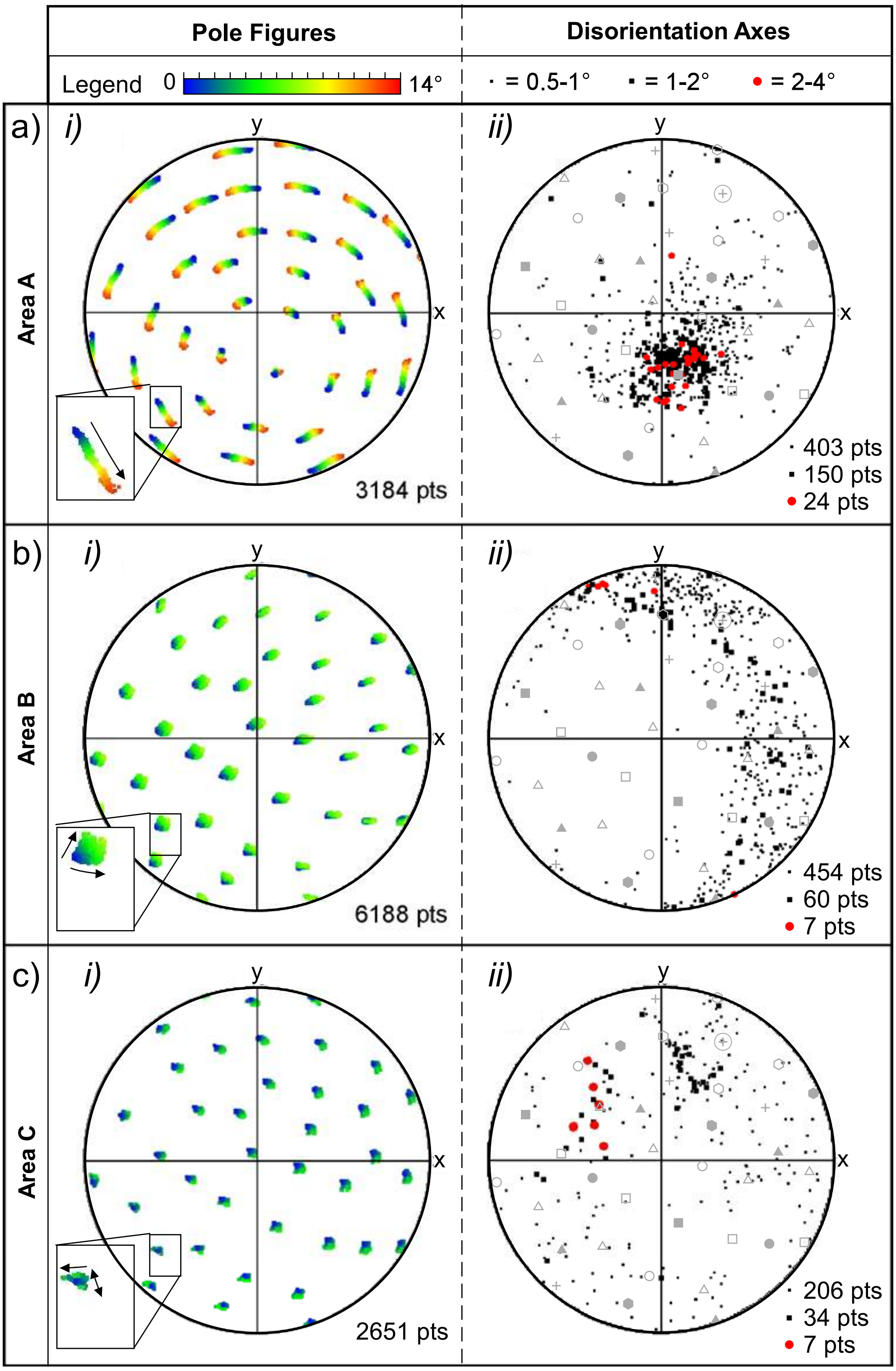

Reddy et al. / Zircon microstructure Figure 4

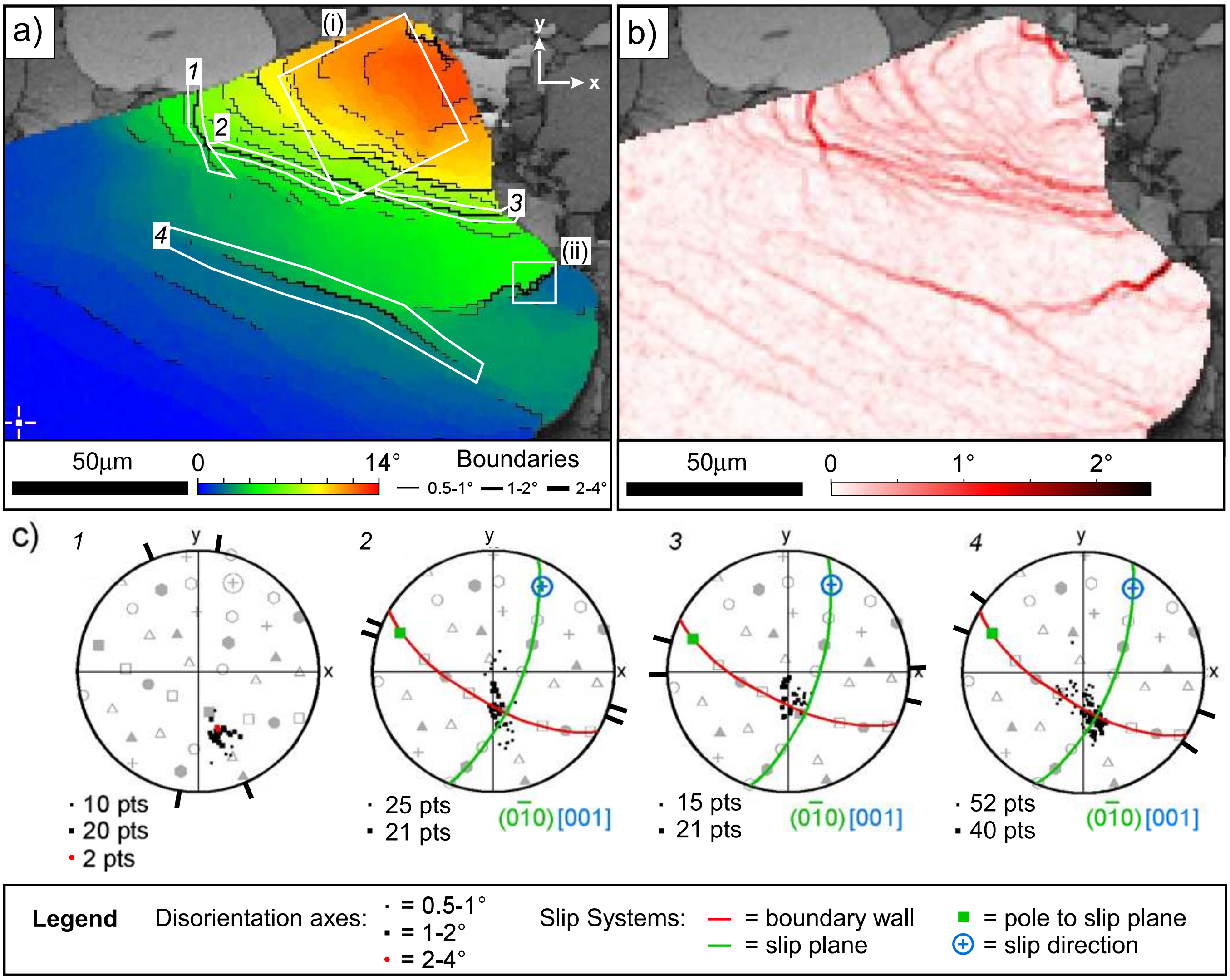

Reddy et al. / Zircon microstructure Figure 5

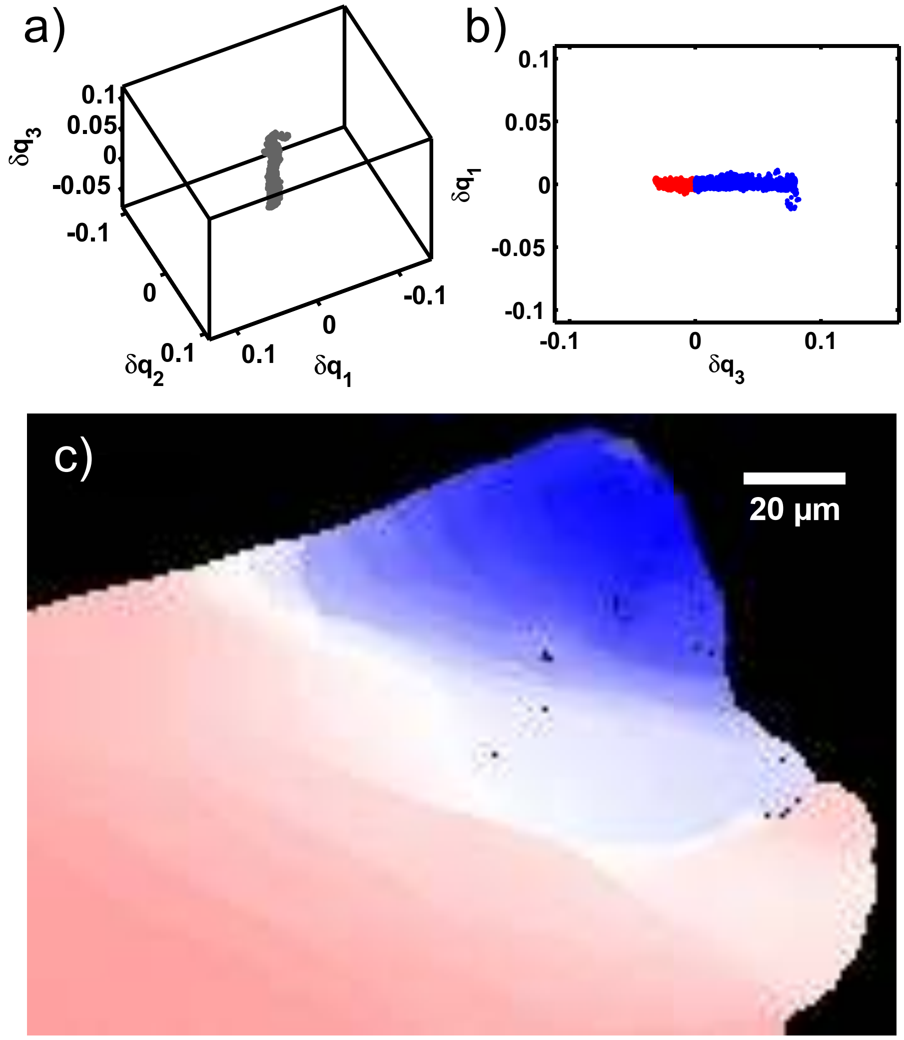

Reddy et al. / Zircon microstructure Figure 6

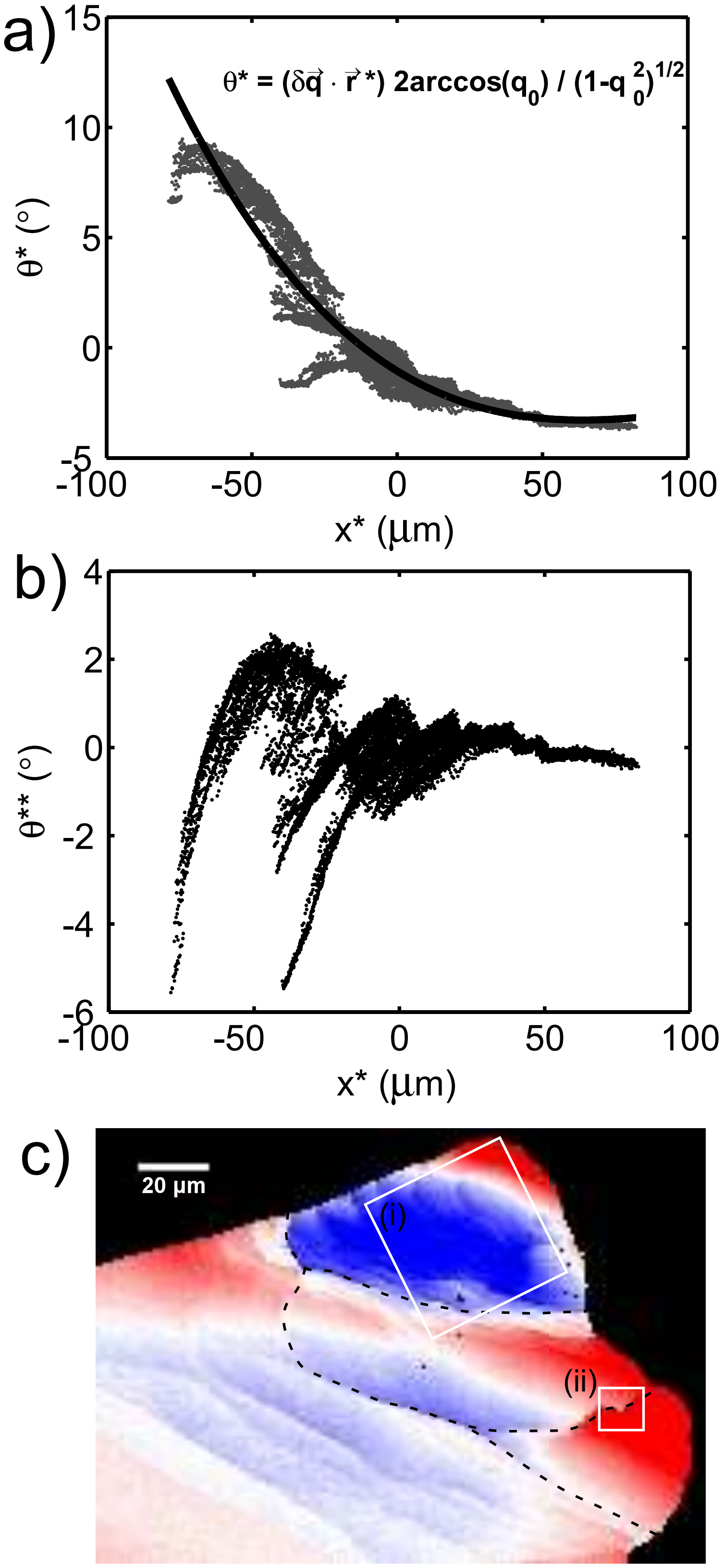

Reddy et al. / Zircon microstructure Figure 7

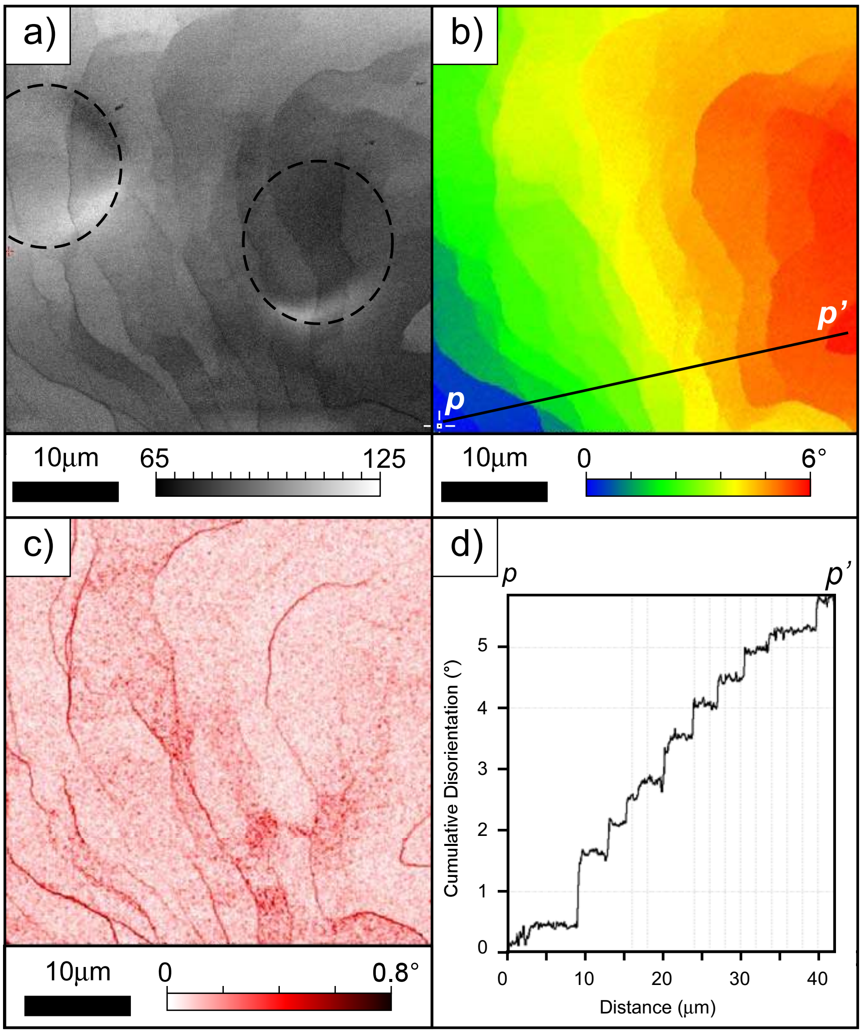

Reddy et al. / Zircon microstructure Figure 8

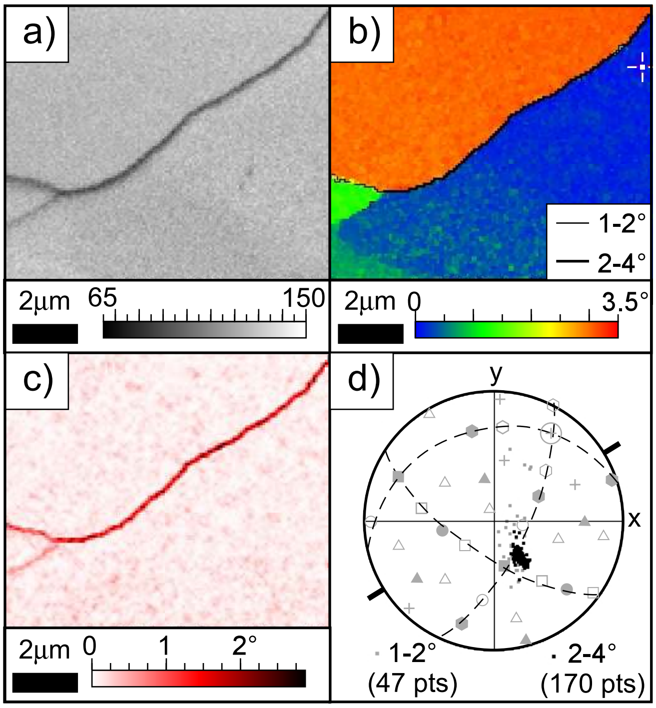

Reddy et al. / Zircon microstructure Figure 9

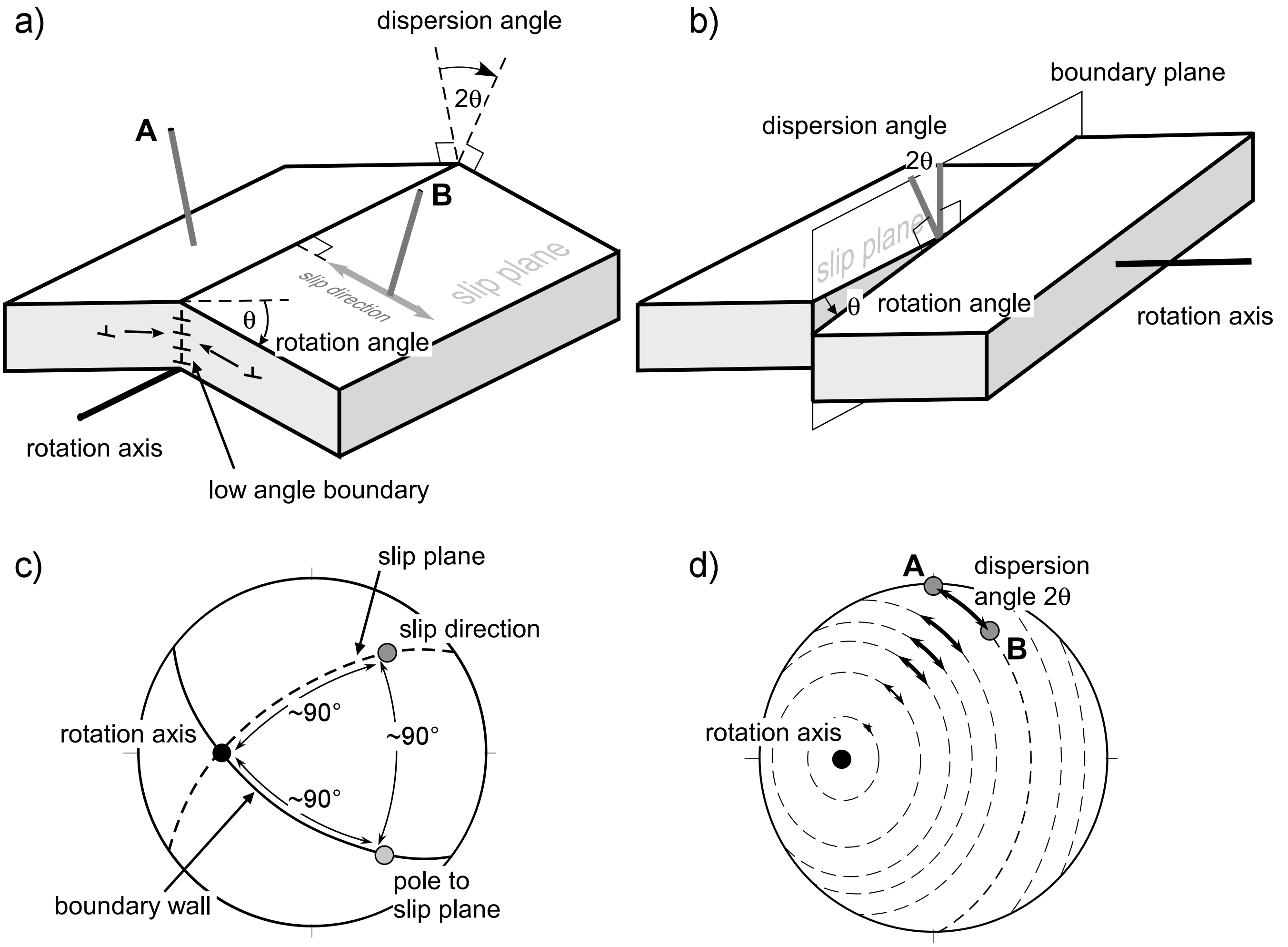

Reddy et al. / Zircon microstructure Figure 10

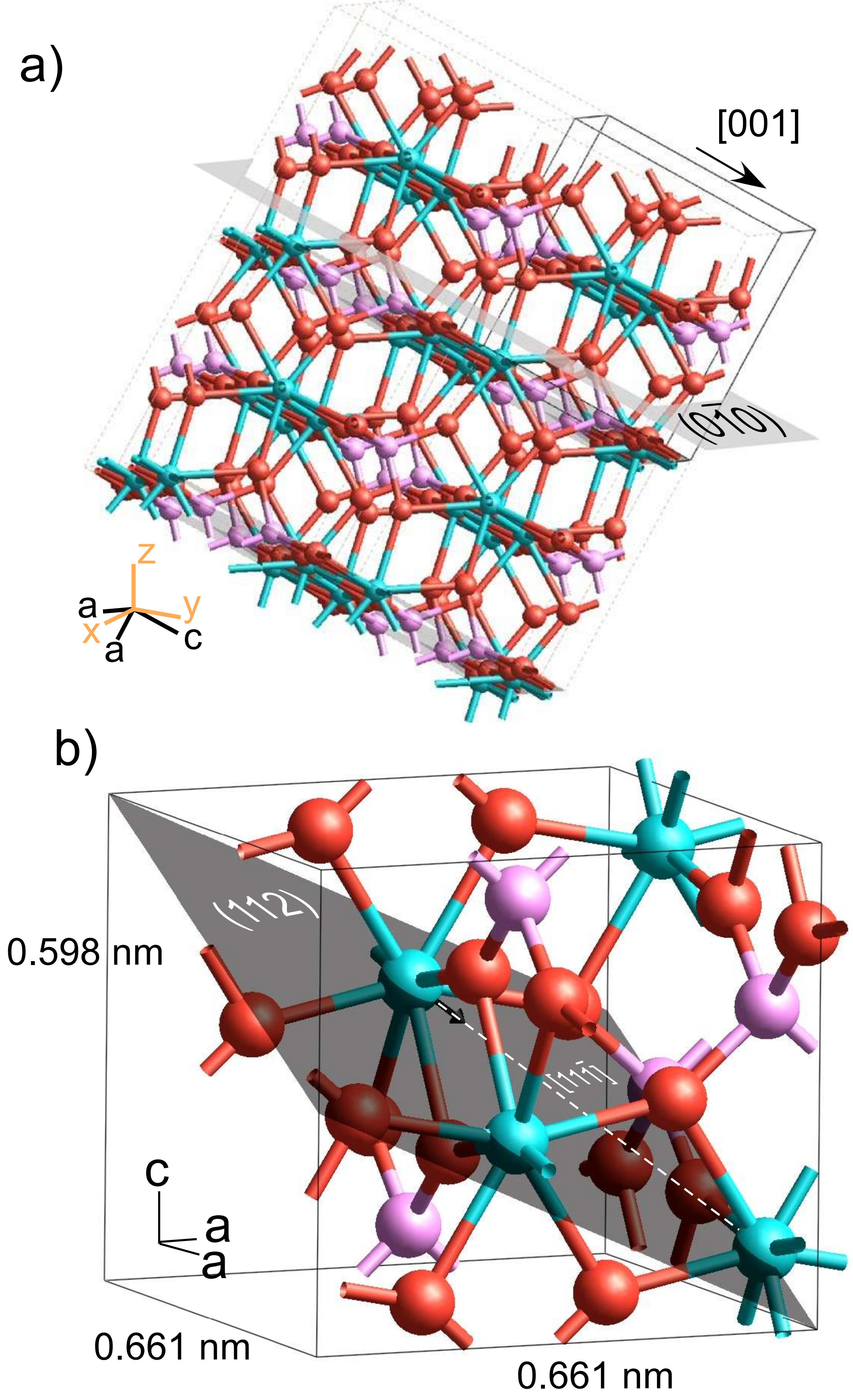

Reddy et al. / Zircon microstructure Figure 11

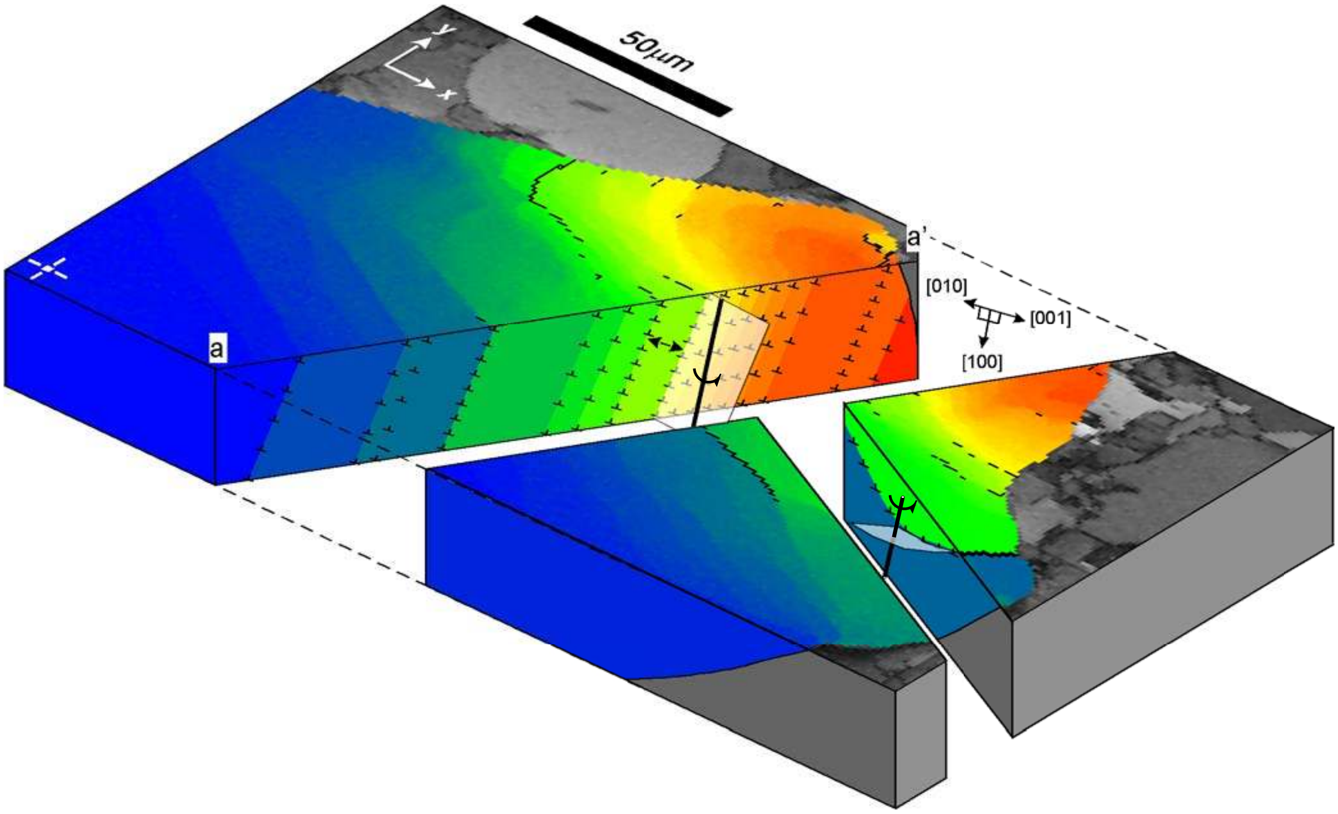

Reddy et al. / Zircon microstructure   Figure 12

Observed microstructure	**Slip system**	**Burgers vectors**	**Active glide systems**	**Deformation conditions**	**Analytical technique**	**Reference**
Abundant straight dislocations	<100> {010}	[100] and [010]	[100](010) and [010](100)	Shocked to 20 GPa and 40 GPa	TEM	Leroux et al. (1999)
Shock induced brittle microfractures	Parallel to (100), (010), and (111)	n/a	n/a	Shocked to 20 GPa and 40 GPa	TEM	Leroux et al. (1999)
Screw dislocations at crack tips of {111} fractures	<110>{111}?	<110>	<110>{111} and <100>{010}	Shocked to 20 GPa and 40 GPa	TEM	Leroux et al (1999)
Phase transformation to scheeite	Martensitic, $\{100\}_z//\{112\}_s$ and $[001]_z//<110>_s$		n/a	Shocked to 40 GPa and 60 GPa	TEM	Leroux et al. (1999)
Dominant cleavage	Parallel to {110}	n/a	n/a	Brittle fracture		Spear, (1982)

Reddy et al / Zircon Microstructure
Table 1

EBSD settings *Figure*	**1c, d; 3**	**5-7**	**8**	**9**
SEM	LEO	XL30	XL30	XL30
EBSP collection time per frame (ms)	14	60	60	60
Background (frames)	64	64	64	64
EBSP noise reduction (frames)	5	4	4	4
(binning)	4x4	4x4	2x2	4x4
(gain)	low	low	low	low
O-lock mode	no	Level 4	n/a	Level 4
Hough resolution	80	60	60	60
Band detection min/max	6/7	6/10	6/8	6/10
X steps	562	172	400	130
Y steps	540	123	400	110
Step distance (µm)	3	1	0.1	0.75
Average mean angular deviation (zircon)	0.6976	0.3702	0.4171	0.4726
Zero solutions (%)	25.56	26.52	0.78	2.54
Noise reduction – 'wildspike'	Yes	Yes	Yes	Yes
- *n* neighbour zero solution extrapolation	5	5	5	5
Kuwahara Filter	3x3 / 5° / 1°	3x3 / 5° / 1°	3x3 / 5° / 1°	3x3 / 5° / 1°
SEM settings *SEM system*	**LEO FEG-SEM**		**Philips XL30 FEG SEM**	
EBSD system	HKL Channel 5		HKL Channel 5	
C coat	No		Yes	
Acc. Voltage (kV)	20		20	
Working distance (mm)	10		20	
Spot size (nm)	~20		~20 (Spot size 5)	
Probe current (nA)	5-10		?	
Vacuum	15-20Pa		4 x 10^{-5} Torr	
Tilt (degrees)	70		70	

Reddy et al. / Zircon microstructure Table 2

a (nm)	0.6604
c (nm)	0.5980
Space Group	I4_1$_{/amd}$
Varient	2
Zr x/a	0.000
Zr y/b	0.750
Zr z/c	0.125
Si x/a	0.000
Si y/b	0.750
Si z/c	0.625
O x/a	0.000
O y/b	0.066
O z/c	0.195
Unit Cell Volume (nm^3)	0.2608

Reddy et al / Table 3

Appendix 1: Unit quaternions

Orientations can be described by a rotation with an angle ω around an axis $\vec{r}$ from a reference orientation. This information can be combined into a unit quaternion

$$q = \begin{pmatrix} q_0 \\ \vec{q} \end{pmatrix} = \begin{pmatrix} \cos(\omega/2) \\ \vec{r}\sin(\omega/2) \end{pmatrix} \tag{A1.1}$$

The elements of the unit quaternion in the convention used here (Morawiec 2003) can also be found from the commonly used Euler angles $(\varphi_1, \Phi, \varphi_2)$

$$\begin{aligned} q_0 &= \left|\cos(\Phi/2)\right| \left|\cos((\varphi_1+\varphi_2)/2)\right| \\ q_1 &= -\operatorname{sgn}\left(\cos(\Phi/2)\cos((\varphi_1+\varphi_2)/2)\right)\sin(\Phi/2)\cos((\varphi_1-\varphi_2)/2) \\ q_2 &= -\operatorname{sgn}\left(\cos(\Phi/2)\cos((\varphi_1+\varphi_2)/2)\right)\sin(\Phi/2)\sin((\varphi_1-\varphi_2)/2) \\ q_3 &= -\operatorname{sgn}\left(\cos(\Phi/2)\cos((\varphi_1+\varphi_2)/2)\right)\cos(\Phi/2)\sin((\varphi_1+\varphi_2)/2) \end{aligned} \tag{A1.2}$$

Appendix 2: Calculation of Dislocation Energy in Zircon

The line energy of a dislocation in an anisotropic medium

$$E_L = \frac{Kb^2}{4\pi}\ln(b/R) \tag{A2.1}$$

is determined by its Burgers vector and an effective energy factor K which depends on the elastic constants C$_{ij}$. For zircon, Burgers vectors of a-type ($\vec{b}_a = [010]a$) are longer then Burgers vector of c-type ($\vec{b}_c = [001]c$). The effect of the elastic anisotropy has previously been investigated in cubic and hexagonal crystals (Foreman 1955). Under particular constraints on the elastic constants, Foreman has obtained a general result for dislocation lines along the third axis and an arbitrary Burgers vector $b = [b_1, b_2, b_3]$ (cf. Figure)

$$\begin{aligned} Kb &= K_1 b_1 + K_2 b_2 + K_3 b_3 \\ K_1 &= (\bar{c}_{11} + c_{12})\sqrt{\frac{c_{66}(\bar{c}_{11} - c_{12})}{c_{22}(\bar{c}_{11} + c_{12} + 2c_{66})}} \\ K_2 &= \sqrt{\frac{c_{22}}{c_{11}}}K_1 \\ K_3 &= \sqrt{c44c55} \\ \bar{c}11 &= \sqrt{c11c22} \end{aligned} \tag{A2.2}$$

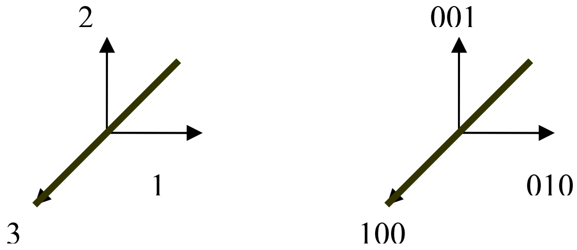

Figure A2.1. Sketch of the geometries involved (left) Foreman and (right) our geometry with dislocation line along [100].

For analyzing dislocations along the crystallographic [100] direction, the coordinate system must be rotated. The resulting matrix of elastic constants in the new system (1=[010], 2=[002], 3=[100])

$$c=\begin{pmatrix} C_{11} & C_{13} & C_{12} & 0 & 0 & 0 \\ C_{13} & C_{33} & C_{13} & 0 & 0 & 0 \\ C_{12} & C_{13} & C_{11} & 0 & 0 & 0 \\ 0 & 0 & 0 & C_{44} & 0 & 0 \\ 0 & 0 & 0 & 0 & C_{66} & 0 \\ 0 & 0 & 0 & 0 & 0 & C_{44} \end{pmatrix} \tag{A2.3}$$

satisfies Foreman's necessary condition (his equation (26)) and the energy factors can be obtained

$$\begin{aligned} K_1 &= (\bar{c}_{11}+C_{13})\sqrt{\frac{C_{44}\left(\bar{c}_{11}-C_{13}\right)}{C_{33}\left(\bar{c}_{11}+C_{13}+2C_{44}\right)}} \\ K_2 &= \sqrt{\frac{C_{33}}{C_{11}}}K_1 \\ K_3 &= \sqrt{C_{44}C_{66}} \\ \bar{c}_{11} &= \sqrt{C_{11}C_{33}} \end{aligned} \tag{A2.4}$$

These expressions allow calculation of the line energy of all dislocation with line vector [100] independent of their Burgers vector. The energy factors for the two possible edge dislocations become

$$\begin{aligned} K_c &= K_2 && \text{for } b_c = [001]c \\ K_a &= K_1 = \sqrt{\frac{C_{11}}{C_{33}}}K_2 && \text{for } b_a = [010]a \\ K_a &= \sqrt{\frac{C_{11}}{C_{33}}}K_c \end{aligned} \tag{A2.5}$$

Both values differ only by a factor given by the ratio between the main elastic constants C_{11} and C_{33}. Elastic constant data for zircon shows considerable variation (Bhimasenachar and

Venkataratnam 1955; Rhyzova et al. 1966; Ozkan et al. 1974)(see Table A2.1), even if the discredited values of Bhimsenachar & Venkataratnam (1955) are ignored (Sirdeshmukh and Subhadra 2005). However, the conclusions for the line energy are consistent.

C_{11}	C_{33}	$(C_{11}/C_{33})^{1/2}$	**Source**
5.7	4.6	1.11	Bhimsenachar & Venkataratnam (1955)
33.01	38.05	0.93	Ryzhova et al. (1966)
42.37	49.00	0.93	Ozkan et al. (1974)

Table A2.1: Comparison of published c11 and c33 elastic properties for zircon.

With the ratio $b_a/b_c = 6.61/5.98 = 1.1$ between the lengths of the two Burgers vectors, the ratio between the line energies of the dislocations becomes

$$\frac{E_a}{E_c} = \frac{K_a b_a^2}{K_c b_c^2} = 0.93 \cdot (1.10)^2 = 1.14 \qquad \text{(A2.6)}$$

and the dislocations of [010]a type have higher line energy.

Furthermore, the energy of a boundary of given disorientation angle (formed by edge dislocations in spacing h)

$$E_B = \frac{E_L}{h} = -\frac{Kb}{4\pi}\theta \ln(\theta) \qquad \text{(A2.7)}$$

depends only linearly on the Burgers vector. The ratio between the boundary energies

$$\frac{E_a}{E_c} = \frac{K_a b_a}{K_c b_c} = 0.93 \cdot (1.10) = 1.02 \qquad \text{(A2.8)}$$

decreases the energy advantage of the [001]c dislocations, but the boundary energy of the [010]a type still remains larger. For this reason [001]c dislocations should be energetically favorable.